

Polyphase tectonic, thermal and burial history of the Vocontian basin revealed by U-Pb calcite dating

3 Louise Boschetti¹, Malou Pelletier¹, Frédéric Mouthereau^{1,2}, Stéphane Schwartz³, Yann
4 Rolland^{3,4}, Guilhem Hoareau⁵, Thierry Dumont³, Dorian Bienveignant³, Abdeltif Lahfid⁶

1. Géosciences Environnement Toulouse, Université de Toulouse Paul Sabatier, CNRS, IRD, 14 av. Edouard Belin, 31400 Toulouse, France
2. Institut Universitaire de France, F-75005 Paris, France
3. ISTerre, Université Grenoble Alpes, USMB, CNRS, IRD, UGE, 38000 Grenoble, France.
4. EDYTEM, Université Savoie Mont Blanc, CNRS, UMR 5204, Le Bourget du Lac, France.
5. Université de Pau et des Pays de l'Adour, E2S UPPA, CNRS, LFCR, UMR5150, Pau, France.
6. BRGM, B.P. 6009, 45060 Orléans Cedex, France

Corresponding author: louise.boschetti@univ-tlse3.fr

Abstract

The Vocontian Basin in southeastern France records a long-lived history of subsidence and polyphase deformation at the junction of Alpine and Pyrenean orogenic systems. This study aims to reconstruct the tectonic, burial and thermal evolution of this basin, based on new U–Pb dating of calcite from veins and faults combined with new RSCM thermometry and stratigraphy-based burial models. Three main generations of calcite are identified: (1) the Late Cretaceous to Paleocene period related to the Pyrenean-Provençal convergence (~84–50 Ma); (2) the Oligocene period linked to the extension of the West European Rift (~30–24 Ma); and (3) the Miocene period, ascribed to strike-slip and compression associated with the Alpine collision (~12–7 Ma). No older ages related to the Jurassic and Early Cretaceous rifting phase are obtained, despite targeted sampling near normal faults, suggesting focused syn-rift fluid circulation or dissolution of early calcite mineralization during subsequent tectonic events. RSCM data highlight a pronounced east–west thermal gradient. Peak temperatures are below 100°C in the west and exceed 250°C in the eastern basin, reflecting greater crustal thinning and/or salt diapirism in the eastern Vocontian Basin with the overlapping Jurassic and

33 Cretaceous rifting phases. These results emphasize the significant impact of the West European
34 Rift in south-eastern France. They further highlight the potential mismatch between large-scale
35 tectonic processes and the tectonic history inferred from calcite U–Pb dating, which is sensitive
36 to the presence of fluids and the physical conditions required for their preservation.

37

38 **1. Introduction**

39 Sedimentary basins in the external part of orogenic belts offer critical insights into the
40 polyphase evolution of plate boundaries. The Vocontian Basin is located at the front of the
41 southern Alpine belt in southeastern France (Fig. 1, 2A). This region recorded a succession of
42 tectonic events from the Mesozoic to the Cenozoic (Roure et al., 1992; Homberg et al., 2013;
43 Mouthereau et al., 2021). They are attributed to Mesozoic rifting in the Alpine Tethys and the
44 Atlantic-Pyrenean systems, Cenozoic inversion during the Pyrenean-Provence collision, and
45 Eocene-Miocene extension associated with the West European Rift and the opening of the Gulf
46 of Lion (e.g., Stämpfli, 1993; Homberg et al., 2013; Bestani et al., 2016; Espurt et al., 2019;
47 Célini et al., 2023). Details of the tectonic evolution of the Vocontian Basin specifically, at the
48 intersection between the Europe-Iberia and Europe-Adria plate boundaries, are however
49 debated. There has been a long-standing debate on whether the Mid-Cretaceous Vocontian
50 Basin is part of a continuous rift linking the Valaisan Basin and the Alpine Tethys to the
51 Pyrenean Basin and Atlantic Ocean (Trümpy, 1988; Stämpfli, 1993; Stämpfli and Borel, 2002;
52 Turco et al., 2012), or if it belongs to the broader Pyrenean/Atlantic rift system. (Debelmas,
53 2001; Manatschal and Muntener, 2009; Angrand and Mouthereau, 2021; Célini et al., 2023;
54 Boschetti et al., 2025a,b). Despite structural and sedimentary evidence of mid-Cretaceous syn-
55 depositional normal faulting in the basin (e.g., Homberg et al., 2013), brittle deformation lacks
56 precise geochronological data. Establishing this chronology is critical, as the Cretaceous
57 extension often overlaps with the onset of Pyrenean compression (Fig. 2B) and could also be
58 linked to diapirism (Bilau et al., 2023b). It is also unclear whether this part of the Alpine
59 foreland was tectonically affected by the Eo-Oligocene West European Rift extension seen
60 nearby in Valence and Manosque basins (e.g., Ford and Lickorish, 2004), or with the opening
61 of the West Mediterranean well identified in the thermal record of the Maures-Esterel massif,
62 a few tens of kilometers to the south ((Fig. 2B) (Boschetti et al., 2023; 2025a,b). These Cenozoic
63 thinning events may have impacted the thermal evolution of the Vocontian Basin and be
64 confused with Mid-Cretaceous extension or Alpine thickening (Fig. 2B) (e.g., Célini et al.,
65 2023). In addition, two north-south compressional events dated to Eocene and late Miocene are
66 recognized in the fault pattern of Provence (Bergerat et al., 1987; Lacombe and Jolivet, 2005).

67 The role of all these major tectonic phases in the brittle deformation history and in the related
68 thermal regime remains unclear as recent studies in the basin have not yet successfully isolated
69 the effects of each geodynamic event. In particular, the temperatures reconstructed based on
70 Raman Spectroscopy of Carbonaceous Material (RSCM) support two alternative tectonic
71 scenarios. (i) Temperatures from the Digne Nappe reflect crustal thickening below the
72 propagating Alpine nappe stack (Balansa et al., 2023). Alternatively, a model involving
73 two superimposed phases of crustal thinning in the Vocontian basin has been proposed (Célini
74 et al., 2023; Fig. 2B). The first phase, in the Upper Jurassic, coincides with the Alpine Tethys
75 opening, while the second, characterised by temperatures exceeding 300°C in the Lower
76 Cretaceous, is associated with Pyrenean rifting and Valaisan opening (Célini et al., 2023).
77 Basin-scale geochronological and thermal analyses are needed to validate this tectonic
78 interpretations. This study addresses these questions by combining basin-scale U-Pb dating of
79 calcite in faults and veins, which origins are constrained by paleostress inversions, with new
80 RSCM temperatures and the analysis of the burial history of the Vocontian Basin. Our aim is
81 to establish a robust chronological framework for the Vocontian basin in the context of the
82 geodynamics of south-east France, and to clarify the sequence and extent of the successive
83 tectonic phases. These constraints improve our understanding of polyphase deformation at the
84 Europe-Iberia-Adria plate boundary.

85

86 **2. Geological setting**

87 Positioned at the front of the Western Alps, the Vocontian Basin forms part of the Southern
88 Subalpine belt, which developed through the interactions between the Pyrenean-Provençal belt
89 to the south and the Alpine belt to the east (Philippe et al., 1998; Balansa et al., 2022; Célini et
90 al., 2024; Fig. 1). It includes the Diois-Baronnies region, and is bordered by the Rhône Valley
91 and the French Massif Central basement to the west, the External Crystalline Massif of Pelvoux
92 to the east, the Vercors Massif to the north, and the Provençal Platform to the south (Figs. 1,
93 2A). The Vocontian Basin contains a thick Mesozoic sedimentary succession, reaching up to
94 7,000 m in its center and 2,600 m along its margins (Fig. 2B). The base of the folded
95 stratigraphic sequence comprises Upper Triassic evaporites, which have resulted in the
96 formation of salt diapirs (e.g. Suzette and Propiac diapirs) that pierce the overlying sedimentary
97 cover and locally control thickness variations (Fig. 3A) (Célini, 2020 and references therein).
98 Basin subsidence began with the opening of the Alpine Tethys during the Early to Middle
99 Jurassic (e. g. Lemoine et al., 1986). This period is marked by the deposition of alternating
100 shallow marine limestones and marls, followed by progressive deepening that culminated with

101 the deposition of organic-rich black shales of the “Terres Noires” formation during the
102 Bathonian–Oxfordian (Fig. 2). In the Late Jurassic, the basin underwent NNE–SSW-directed
103 extension, recorded by syn-sedimentary NNW–SSE-trending normal faults (Homberg et al.,
104 2013). This extensional regime, linked to the propagation of the Alpine Tethys, led to the
105 deposition of fine-grained bioclastic Tithonian limestones, which serves as a distinctive
106 morphostructural marker and reflect slower subsidence (Remane, 1970; Joseph et al., 1988).
107 The subsidence continued through the Early Cretaceous (Valanginian–Aptian), with the
108 deposition of alternating layers of marls and limestones that define the deeper marine
109 “Vocontian facies”, contrasting with shallow-water carbonates of the Vercors and Provence
110 platforms, known as the "Urgonian facies" (Fig. 2A).

111 A major tectonic shift occurred during the Aptian–Albian, characterised by increased
112 subsidence and the deposition of thick marly sequences ("Blue Marls"; Debrand-Passard et al.,
113 1988) (Fig. 2B). This phase is associated with the development of E–W-trending normal faults,
114 suggesting a reorientation of the extensional stress field from NNE–SSW (Late Jurassic) to
115 WNW–ESE (Homberg et al., 2013). This shift likely reflects plate tectonic reorganization,
116 linked to the onset of Europe–Iberia divergence (Bay of Biscay opening) and the closure of the
117 Alpine Tethys through Europe-Adria convergence (Lemoine et al., 1987; Stämpfli, 1993).

118 During the Late Cretaceous, sandstones deposition dominated in the east of the basin, while
119 limestones prevailed in the west (Fig. 2). In the north-eastern part of the basin, at the current
120 location of the Dévoluy massif, a stratigraphic hiatus spanning the Turonian, Coniacian to the
121 Santonian (Fig. 3B) is documented, regionally referred to as the Turonian unconformity (e. g.
122 Flandrin, 1966). This interval is characterized by the argillaceous to sublithographic lower
123 Cretaceous limestones and E-W-trending folds, which lie in direct contact, below an erosional
124 surface, with Campanian-Maastrichtian bioclastic and terrigenous deposits (Fig. 2-3B; Gidon
125 et al., 1970; Arnaud et al., 1974). Across the Vocontian basin, the main stratigraphic hiatus
126 corresponds to the Paleocene-Early Eocene (Fig. 2B). This late Cretaceous-Paleocene event
127 coincides with the onset of Iberia-Europe convergence, marking the initial stages of the
128 Pyrenean-Provençal orogeny (~84 Ma; Angrand and Moutherau, 2021; Moutherau et al.,
129 2014; Muñoz, 1992; Teixell et al., 2018; Ford et al., 2022) and is consistent with the exhumation
130 of the Pelvoux crystalline basement to the northeast at ~85 Ma (Fig. 2; Boschetti et al., 2025a).

131 Following this tectonic change, marine incursions were limited and localized from the Late
132 Eocene to the Miocene (Fig. 2B). This period corresponds to the early Alpine collision, which
133 affected the internal domains and the eastern parts of the External Crystalline Massifs (e. g.
134 Simon-Labric et al., 2009; Boschetti et al., 2025c). Meanwhile, regional-scale extension

135 developed in the European plate, driven by the Western European Rift system and the opening
136 of the Liguro–Provençal back-arc basin in southeastern France (Fig. 1) (Hippolyte et al., 1993;
137 Séranne et al., 2021; Jolivet et al., 2021; Boschetti et al., 2023). In the eastern basin, the latest
138 compressional phase is recorded by N–S to NW–SE-trending structures associated with the
139 Digne thrust (Fig. 1-2) and final Alpine exhumation between ~12 and 6 Ma (Schwartz et al.,
140 2017).

141

142 **3. Sampling and methods**

143 **3.1 Sampling strategy**

144 Sampling sites were carefully selected to characterize both the nature and ages of brittle
145 deformation in the Jurassic and Cretaceous formations of the Vocontian Basin (Fig. 2A). We
146 first targeted sites where normal faults were described as syn-rift faults or veins formed shortly
147 after deposition (Homberg et al., 2013), and where we observed calcite mineralizations. The
148 analysis of these specific sites was expanded to include other types of brittle structures, such as
149 strike-slip and reverse faults, to document the polyphase deformation of the Vocontian Basin.
150 Our sampling targets were further guided using the 1:50.000 scale BRGM geological maps
151 from Die to Sisteron.

152

153 **3.2 Tectonic and paleostress analysis**

154 To reconstruct the tectonic evolution of brittle deformation in the Vocontian Basin, fault-slip
155 data and other stress indicators, including calcite veins, were measured in the field and collected
156 for U-Pb dating. Local stress states were inferred by inverting fault-slip data following the
157 methodology of Angelier (1990) using the Win-Tensor software (Delvaux and Sperner, 2003).
158 This analysis provided the orientation of the three principal stress axes (σ_1 , σ_2 , and σ_3) and the
159 shape of the stress ellipsoids defined by the ratio $\phi = \frac{\sigma_2 - \sigma_3}{\sigma_1 - \sigma_3}$, reflecting the relative magnitudes
160 of the principal stresses. Relative chronology of the reconstructed stress tensors was determined
161 from cross-cutting relationships between successive generations of veins and faults (normal,
162 reverse, or strike-slip faults). Chronology relative to folding was refined by comparing the
163 orientation of faults, veins, and/or associated stress states in their present-day and unfolded
164 configurations. This approach assumes that faults originally formed according to an
165 Andersonian state of stress, with one principal stress axis vertical.

166

167 **3.3 Calcite U-Pb geochronology**

168 Prior to U-Pb analyses, each polished thick section was petrographically characterized at IPRA
169 (Institut Pluridisciplinaire de Recherche Appliquée) in Pau, France. This involved optical
170 microscopy coupled with cathodoluminescence (CL) imaging to identify multiple calcite
171 generations (Supplementary Material Fig. S1). CL images were acquired using an OPEA
172 Cathodyne system coupled with a Nikon BH2 microscope, operating at an acceleration voltage
173 of 12.5 kV and an intensity of 300–500 mA. U-Pb dating of calcite was performed at IPREM
174 laboratory (Institut des Sciences Analytiques et de Physico-Chimie pour l'Environnement et les
175 Matériaux), following the protocol of Hoareau et al. (2021, 2025). This method employs
176 isotopic mapping of U, Pb, and Th via a continuous ablation process, combined with a virtual
177 spot method to construct Tera-Wasserburg (TW) plots (Hoareau et al., 2021, 2024, 2025).
178 Detailed analytical procedure and data processing is provided in the Supplementary Material 1
179 (Tabs. A1-A2). The setup used a 257 nm femtosecond laser ablation system (Lambda3, Nexeya,
180 Bordeaux, France), operating at a frequency of 500 Hz with a spot size of 15 μm . Ablation was
181 conducted in a controlled atmosphere composed of helium (600 mL/min) and nitrogen (10
182 mL/min), mixed with argon in the ICPMS. This system was coupled to an HR-ICPMS Element
183 XR (ThermoFisher Scientific, Bremen, Germany) equipped with a jet interface (Donard et al.,
184 2015).

185

186 **3.4 Burial history**

187 The subsidence history of the Vocontian Basin was reconstructed using stratigraphic sections,
188 including thicknesses and lithologies, from the 1:50.000 scale geological maps of Die, Mens,
189 Dieulefit, Luc-en-Diois, Gap, Nyons, Serres, Laragne-Montéglise, Vaison-la-Romaine, and
190 Séderon, providing basin-wide coverage (Fig. 4). Standard backstripping techniques (Allen and
191 Allen 2013) were applied. The sedimentary units were first decompacted using coefficients
192 appropriate to their dominant lithology (limestone, marl or clay), with stratigraphic ages
193 inferred from the geological maps. To enable comparison between stratigraphic columns, the
194 stratigraphic data were resampled at 1 Myr intervals, grouped into 5 Myr bins, and interpolated
195 using the 2D spline method.

196

197 **3.5 RSCM thermometry approach**

198 To determine the peak temperatures reached by sediments in the Vocontian Basin, RSCM
199 analyses were conducted on an initial set of Middle to Upper Jurassic and Lower Cretaceous
200 carbonate samples collected near U-Pb dated calcites (Fig. 2A, 4). A second set of samples was
201 collected further east, in or near, the Authon-Valavoire thrust nappe, a parautochthonous unit at

202 the front of the Digne nappe, where deeper Lower Jurassic strata of the Vocontian are exposed
203 and diapirism has occurred (e.g., Célini et al., 2024). The RSCM approach constrains thermal
204 processes ranging from advanced diagenesis to high-grade metamorphism, covering
205 temperatures from 100 to 650°C (e.g., Ayoa et al., 2010; Koukestu et al., 2014; Schito et al.,
206 2017). Appropriate calibrations depend on the temperature range and geological context. Here,
207 we applied the calibration of Lahfid et al. (2010) was applied for temperatures between 200 and
208 340°C, and the qualitative approach of Saspiurry et al. (2020) for temperatures between 100
209 and 200°C. Analyses were performed at the Bureau de Recherches Géologiques et Minières
210 (BRGM; Orléans, France) using a Horiba LABRAM HR instrument with a 514.5 nm solid-
211 state laser source. The laser was focused with a BxFM microscope using a x100 objective with
212 a numerical aperture of 0.90 and under 0.1 mW at the sample surface.

213

214 **4. Results**

215 **4.1 Microtectonics and paleostress reconstructions**

216 Veins and striated planes associated with folds (Fig. 5A), reverse faults (Fig. 5B) and normal
217 faults (Fig. 5C) were measured and sampled. Stereograms of beddings, fault-slip data, veins
218 and, when relevant, their associated back-tilting state of stress, are presented in Figure 6. When
219 sufficient fault-slip data were available for inversion (minimum of four), the calculated stress
220 axes are reported (Fig. 6; Table 1). In this section, data from samples VOC-23-09a to VOC-23-
221 16d are presented in numerical order, followed by samples BON-23-01 to 03, and GLAN-23-
222 02, which belong to a second, separate field campaign. No measurements were conducted for
223 samples VOC-23-01a and VOC-23-01b, as the sampling area lies within the diapiric structure
224 of the Dentelles de Montmirail (Figs. 2A and 6), potentially introducing local complexities.
225 The sampling area of sample VOC-23-09b is dominated by strike-slip faults, with paleostress
226 inversion indicating a strike-slip regime under NW-SE compression (Fig. 6). At the VOC-23-
227 11a site, where bedding is flat, paleostress reconstructions also reveal a strike-slip regime,
228 involving NE-SW compression and NW-SE extension (Figs. 5B, 6).

229 Samples VOC-23-12a and VOC-23-12b record distinct deformation patterns. VOC-23-12a
230 comprises calcite veins indicative of WNW-ESE extension, whereas sample VOC-23-12b
231 exhibits similar calcite veins, together with additional strike-slip deformation, consistent with
232 WNW-ESE compression and NNE-SSW extension (Fig. 6). This stress orientation closely
233 matches that of VOC-23-09a and b sites. The geometry of the stress axes relative to bedding
234 dip and orientation suggests that this state of stress postdates folding.

235 At the VOC-23-13 site, strike-slip faults indicate a paleostress regime characterized by N-S-
236 directed compression and E-W-directed extension (Figs. 5C and 6). Sample VOC-23-14a, a
237 calcite vein spatially associated with sample VOC-23-14b, occurs adjacent to a strike-slip fault
238 with a sinistral component. Paleostress reconstruction indicates a WNW-ESE extension
239 coupled with NNE-SSW compression (Fig. 6).

240 Sample VOC-23-16d shows calcite veins affected by strike-slip deformation. In contrast,
241 sample VOC-23-12b shows only post-vein strike-slip deformation. Paleostress analysis
242 indicates NW-SE-directed extension (Fig. 6). Samples BON-23-01a and BON-23-01b consist
243 of striated calcite affected by layer-parallel shortening (LPS), interpreted as flexural slip related
244 to folding (Lacombe et al., 2021) (Figs. 5A, 6). Sample BON-23-01c, a calcite vein formed
245 within the same fold, is interpreted to have formed during fold growth. Paleostress
246 reconstruction at the Bonneval outcrop indicates N20°E-directed compression associated with
247 the formation of the N110°E-trending fold (Figs. 5A, 6). Finally, the GLAN-23-02 outcrop
248 exhibits a normal fault consistent with NE-SW-oriented extension.

249

250 **4.2 Petrography of calcite samples**

251 In total, 15 samples were dated in this study: 6 veins (VOC-23-01a, 01b, 09b, 12a, 14b and
252 BON-23-03) and 9 striated fault planes (VOC-23-9a, 11a, 12b, 13, 14a, 16d, BON-23-01, 02
253 and GLAN-23-02). Most samples contain blocky to elongate-blocky calcite, ranging from
254 millimetres to centimetres (Fig. 5; VOC-23-01, 9a, 12a, 22b, 13a, 14a, BON-23-01, 02, 03 and
255 GLAN-23-02). These calcites are characterized by homogeneous luminescence, indicating a
256 single-phase growth with no evidence of recrystallization (Figs. 7A, B; Supplementary.
257 Material Fig. S1.). Two samples exhibit distinct calcite morphologies. Sample VOC-23-11a
258 contains a centimetric calcite showing a transitional morphology between syntaxial and
259 stretched crystals (Figs. 7C, D), suggesting variable growth orientations and multiple crack-
260 seal events. Similarly, sample VOC-23-16d displays millimetric to centimetric blocky calcite
261 crosscut by a younger generation of more elongated and stretched calcite (Fig. 7C, D).

262

263 **4.3 Calcite U-Pb geochronology**

264 This study presents 16 new calcite U-Pb ages obtained from eight types of brittle structures
265 (Table 1; Figs. 8, 9, 10). The Tera-Wasserburg diagrams show data well spread along the
266 discordia line, with Mean Squared Weighted Deviation (MSWD) ranging from 1.1 to 1.9,
267 indicating robust and well-resolved age estimates. Three distinct age groups can be identified
268 within the dataset. The first age group corresponds to the Late Cretaceous to Early Eocene

269 interval, based on veins collected in late Jurassic-Early Cretaceous strata in the western part of
270 the basin. In the Dentelles de Montmirail area, ages of 82.9 ± 3.8 Ma (VOC-23-01b) and 76.5 ± 3.4 Ma (VOC-23-01a) were obtained. Further north, in the Die region, fold-related structures
272 associated with N20°E shortening yielded ages of 72.0 ± 3.7 Ma (BON-23-01a), 71.2 ± 8.1 Ma
273 (BON-23-01b), and 50.0 ± 4.3 Ma (BON-23-01c) (Fig. 8).

274 The second age group corresponds to veins and faults formed during the Oligocene. The
275 obtained ages range from 34.3 ± 1.5 Ma (vein: VOC.23.14a), 30.3 ± 1.5 Ma (fault:
276 VOC.23.14b2), 30.0 ± 2.8 Ma (fault: VOC.23.13b), 28.1 ± 1.2 Ma (fault: VOC.23.14b1), 25.6 ± 1.3 Ma (vein: VOC.23.12a), 23.2 ± 1.3 Ma (deformed vein: VOC.23.12a and b) and 27.6 ± 5.4 Ma (fault: GLAN.23.02) (Fig. 9). Most of these fractures correspond to NW-SE to NE-SW
277 extension (Fig. 6). However, sample VOC.23.12b indicates a strike-slip stress regime with
278 NNE-SSW extension and WNW-ESE compression, similar to that inferred from VOC.23.09
279 (Fig. 6). Calcite veins in VOC.23.12b are of the same type as those in VOC.23.12a.

280 The third age group corresponds to Miocene veins and strike-slip faults hosted in Upper
281 Jurassic-lower Cretaceous carbonates. Two subgroups can be distinguished. The first subgroup,
282 dated to 12.2 ± 3.2 Ma and 12.5 ± 5.2 Ma (fault: VOC.23.11a and fault: VOC.23.16d), records
283 a strike-slip regime defined by NE-SW compression and NW-SE extension (Figs. 10, 6). The
284 second subgroup, with ages of 7.8 ± 0.6 Ma and 7.0 ± 2.2 Ma (fault: VOC.23.09a and vein:
285 VOC.23.09b), also reflects a strike-slip regime but with stress orientations indicating NW-SE
286 compression and NE-SW extension (Figs. 10, 6).

289

290 **4.5 RSCM thermometry**

291 RSCM data from the first set of Upper Jurassic and Lower Cretaceous carbonates in the central
292 and southern parts of the study area indicate maximum temperatures below 100°C (VOC-23-
293 01 and VOC-23-16; Table 2). For the second set, reliable temperatures estimates were obtained
294 for 12 samples using an appropriate calibration (Table 2, Fig. 6), which can be divided in two
295 groups. Temperatures measured in Lower to Upper Jurassic strata near Saint Roman and
296 Montmaure, in the Die area, range between 100 and 180°C (VOC-23-18, VOC-23-17). The
297 lowest temperatures are found near Veynes and close to the Devoluy massif (sample VOC-24-
298 20), in Sigoyer village (samples VOC-23-02, VOC-23-03), and in the upper stratigraphic unit
299 of the Authon-Valavoire nappe (VOC-24-28), and in the eastern part of the basin, below the
300 Digne nappe (sample VOC-24-29). The higher bound of RSCM temperatures, reaching up to
301 170°C, is measured in samples VOC-24-24a and 33, both located near diapiric structures
302 “Rocher de Hongrie” (Célini et al., 2024). These values align with previously reported

303 temperatures of 140-200°C in the vicinity of the same diapir (Célini et al., 2024). The second
304 group characterized by higher temperatures between 215 and 275°C, includes samples located
305 1 km to the south of Sigoyer (VOC-24-23), within the middle Jurassic strata in the hangingwall
306 of the Authon-Valavoire nappe (VOC-24-25), and in the Lias sequence near the Astoin diapir
307 (VOC-23-31). Temperatures of this second group fall within the temperature range recorded in
308 the Authon-Valavoire nappe, particularly near Astoin, closer to the Digne nappe (Célini et al.,
309 2024). To summarize, our data reveal a thermal contrast between the western and eastern
310 domains of the Vocontian Basin. While the organic matter of upper Jurassic-lower Cretaceous
311 formations remains thermally immature, deeper Early-Middle-Late Jurassic formations
312 exposed in the eastern part of the Vocontian basin, close to the Authon-Valavoire and Digne
313 nappes exhibit significantly higher thermal maturity, with RSCM temperatures exceeding
314 180°C and reaching up to 275°C. A similar increase in RSCM temperatures between the Upper
315 Jurassic-Early Cretaceous and deeper stratigraphic units of the Early-Middle Jurassic has also
316 been documented in stratigraphic sections of the Digne Nappe (Célini et al., 2022; Balansa et
317 al., 2023).

318

319 **4.4 Burial histories and temperatures reached in the basin**

320 Burial histories for the Vocontian Basin are presented in Figure 11. Each curve represents the
321 burial evolution within the basin, reconstructed from stratigraphic thicknesses indicated in
322 explanatory notes of the BRGM 1/50.000 geological maps covering the basin. The data indicate
323 that total sediment accumulation reached a maximum of 6-7 km since the Early Jurassic. This
324 is shown by the decompacted thicknesses estimated at 6800 m in the Die region and 5900 m
325 near Nyons, in the northern and western sectors of the basin, respectively. In contrast, areas
326 lacking exposures of Lower Jurassic series such as Vaison-la-Romaine, show reduced total
327 subsidence of around 2500 m. Despite these differences, most parts of the basin recorded a main
328 phase of burial during the Middle Jurassic (Callovian, ~160 Ma), associated with the
329 widespread deposition of marls and shales of the “Terres Noires”, typical of the External Alps.
330 During this period, about 2 km of “Terres Noires” accumulated with rates of 200-400 m/Myr.
331 Following the Middle Jurassic, the burial rates decreased but continued through the Late
332 Jurassic and Early Cretaceous. A second phase of accelerated subsidence took place during the
333 Early Cretaceous, around 130 Ma (Hauterivian), documented in the Mens section by the
334 deposition of about 700 m of marls and limestones (Fig. 4). A third major burial phase, dated
335 to 100-90 Ma (Fig. 11), is recorded in 6 of the 10 stratigraphic sections (Fig. 11). This phase is
336 characterized by increasing siliciclastic influx, revealed by the deposition of 700-800 m

337 alternating sandstones, marls and limestones (e.g., Nyons, Séderon, Vaison-la-Romaine). In
338 contrast, the Gap, Laragne-Montéglon, and Mens sections, however, show evidence of erosion
339 rather than sedimentation at this time. These contrasting depositional patterns reveal concurrent
340 uplift in the source regions and structural compartmentalization in the Vocontian Basin (Fig.
341 11). A last episode of subsidence, reaching 350-500 m (e.g., Die, Laragne) is documented
342 during the Eocene-Oligocene (Fig. 11).

343

344 **5. Discussion**

345 The results from this study are put into perspective of the evolution of the Vocontian Basin of
346 south-east France through time. For this, we merge results from structural analysis with
347 corresponding U-Pb calcite ages, and discuss the evolution of the related burial history
348 estimated from the lithological logs, which have been used to infer paleo-thermal gradients.
349 Four main evolutionary stages can be proposed based on these data, which are discussed below.
350

351 **5.1 The Mesozoic rifting: E-W trend in thermal gradients and low Ca-rich fluid 352 circulation (170-90 Ma)**

353 The Vocontian basin recorded a prolonged phase of subsidence throughout the Jurassic and
354 Cretaceous (Fig. 11), which was not associated with a distinct fluid event. This period coincides
355 with the rifting of the European paleomargin as inferred by the thermal evolution of the Pelvoux
356 Variscan crystalline basement to the north (Boschetti et al., 2025a,c), and from the burial history
357 below the Digne Nappe to the east (Célini et al., 2023). This eastern margin of the basin was
358 likely inverted during the late stages of the Alpine collision between 12 and 6 Ma (Schwartz et
359 al., 2017). We distinguish a first major phase of sedimentary burial that occurred during the
360 Callovian-Oxfordian (170-160 Ma), which postdates the necking of the European paleomargin
361 identified in the External Crystalline Massifs (Mohn et al., 2014; Ribes et al., 2020; Dall'Asta
362 et al., 2022) and is synchronous with the opening of the Alpine Tethys (Lemoine et al., 1986;
363 Manatschal and Müntener, 2009). This rifting is recognized in the Vocontian Basin, where it is
364 expressed by WNW-ESE extension (Dardeau et al., 1988; Homberg et al., 2013), but it is not
365 captured in our calcite U-Pb ages. Similar observations can be made for the subsequent
366 extensional Cretaceous (~135 Ma), for which no faults of that age are reported. The high
367 temperatures measured in the Digne Nappe at this time are interpreted as reflecting renewed
368 extension associated with the opening of the Valaisan domain along the European margin
369 (Célini et al., 2023), consistent with ongoing burial heating recorded in the Pelvoux massif
370 (Boschetti et al., 2025a,c). This thermal peak coincides with a shift from the Middle Jurassic

371 WNW–ESE extension to NNE–SSW extension during the Barremian–Aptian (Dardeau, 1988;
372 de Graciansky and Lemoine, 1988; Homberg et al., 2010). This later extensional phase is
373 recorded not only throughout the Vocontian Basin (Homberg et al., 2013), but also along its
374 margins. Evidence for this later extensional event includes deformation along the Ventoux–
375 Lure fault zone (Beaudoin et al., 1986; Huang et al., 1988), the formation of large-scale sliding
376 domains on the Vercors platform (Bièvre and Quesne, 2004), and subsidence in east-west-
377 oriented domains along the Ardèche margin during the same period (Cotillon et al., 1979). Our
378 RSCM analyses indicate an increase in peak temperatures toward the east of the Vocontian
379 Basin, where deeper Lower Jurassic stratigraphic strata are exposed (Fig. 6; Table 2).
380 Comparing these temperatures with temperature inferred from burial depths using normal
381 (30°C/km) to high (60°C/km) geothermal gradients suggests that the eastern sector experienced
382 unusually high to extreme gradients, consistent with increasing crustal thinning in the Vocontian-
383 Valaisan rift segment this direction (Fig. 6; Table 2). It should be noted that the sharp increase
384 in the geothermal gradients is not solely due to crustal thinning, but is also largely a result of
385 mantle thinning and asthenosphere uplift. The absence of calcite mineralisation in brittle
386 tectonic features at this time, despite specifically targeting potentially related veins, is
387 intriguing. Indeed, evidence of barite, authigenic quartz and pyrite mineralization in the
388 Callovian-Oxfordian shales in the deeper part of the basin is interpreted as reflecting basal fluid
389 flow during syn-rift peak burial in the Middle Cretaceous, as well as brines related to salt diapirs
390 (Guilhaumou et al., 1996). We suggest that the absence of Middle Cretaceous calcites can be
391 explained either by 1) faulting occurring at a depth too shallow for calcite precipitation, 2)
392 subsequent burial to 2-3 km in the eastern basin leading to the dissolution of previous Middle
393 Cretaceous calcites due to changing physical conditions (e.g., pH and temperature). In addition,
394 mechanical decoupling in the Triassic salt layer during extension may have focused fluid flow,
395 so that mineralized fluids of this age are detectable only locally, near the emergence of salt
396 diapirs.

397 A third depositional phase occurred around 100-90 Ma, in agreement with syn-faulting deposits
398 along the Clausis and Glandage fault systems in the Vocontian/Dévoluy basin (Fig. 11, 3)
399 (Gidon et al., 1970; Arnaud et al., 1974) and with strike-slip activity along the Toulourenc faults
400 in the Ventoux-Lure massif (Montenat et al., 2004). Regionally, this tectonic phase coincides
401 with strike-slip movements along the Cévennes, Nîmes and Durance faults (Montenat et al.,
402 2004; Parizot et al., 2022), potentially associated with local compression related to diapiric
403 movement at 95-90 Ma (Bilau et al., 2023b) and normal faulting reported in Provence (Zeboudj
404 et al., 2025). This episode is a response of the continental rifting between Iberia-Ebro and

405 European plates, and the formation of the Pyrenean rift system (Angrand and Moutherau,
406 2021) (Fig. 12A). Strike-slip movements along inherited faults (Cévennes, Nîmes, Durance
407 faults) were associated with oblique extension accommodated by overlapping rift segments in
408 the Pyrenean and Vocontian basins (Fig. 12). This complex tectonic setting likely triggered the
409 emergence of continental blocks that can explain the abundance of sandstone deposits during
410 this period in the Vocontian basin (Fig. 4, 11). This interpretation aligns with the documented
411 formation of an uplifted structure in Provence during the Albian-Cenomanian, known as the
412 Durancian Isthmus (Combes, 1990; Guyonnet-Benaize et al., 2010; Chanvry et al., 2020,
413 Marchand et al., 2021). Cooling and exhumation in the French Massif Central to the west are
414 also documented from 120-90 Ma (Olivetti et al., 2016), which may have contributed to feeding
415 of the Vocontian basin during this period (Fig. 12A). Although this period is synchronous with
416 the onset of Adria/Europe convergence (e.g., Le Breton et al., 2021; Angrand and Moutherau,
417 2021; Boschetti et al., 2025a,b,c), the impact of contraction in the Alps on the evolution
418 Vocontian Basin remains to be assessed.

419

420 **5.2 Post-Mid Cretaceous evolution: U-Pb/calcite dating record of multiple Pyrenean- 421 Provençal collision events (90-34 Ma)**

422 The oldest calcite U-Pb ages of 84.6 ± 2.4 Ma and 77.7 ± 2.9 Ma, reported in the Jurassic strata
423 forming the wall of the Suzette diapir (Dentelles de Montmirail) align with the onset of the
424 Pyrenean-Provençal collision around 84 Ma (Angrand and Moutherau, 2021; Moutherau et
425 al., 2014; Muñoz, 1992; Teixell et al., 2018; Ford et al., 2022). These old calcite ages may
426 reflect halokinetic movement of the Suzette diapir in response to far-field stresses that triggered
427 tectonic inversion and exhumation all over Europe (Moutherau et al., 2021). These ages can
428 also be related to a deformation event in the Dévoluy massif affecting the Early Cretaceous
429 units, linked to E-W-directed folding and erosion dated to Coniacian-Santonian (Fig. 3B) (ca.
430 85 Ma) (Flandrin, 1966; Lemoine, 1972; Gidon et al., 1970; Arnaud et al., 1974), or the end of
431 diapiric movement in southern Provence (Wicker and Ford, 2021). Younger U/Pb ages of 72.0 ± 3.7 Ma
432 and 71.2 ± 8.1 Ma associated with N20°E shortening coincides with the intensification
433 of the Pyrenees exhumation at 75-70 Ma (Moutherau et al., 2014), a phase that is regionally
434 recorded across southeastern France by a cooling event documented from the Pelvoux to the
435 Maures-Tanneron massifs (Fig. 12A) (Boschetti et al., 2025a,b). It is also recognized in the
436 region associated with the sinistral reactivation of the Cévennes fault around 76 Ma (Parizot et
437 al., 2021). The Pyrenean-Provençal collision is therefore well represented in the Vocontian
438 Basin.

439 Our data also resolve a younger N20°E-directed contractional stage dated at 50.0 ± 4.3 Ma (Fig.
440 6) that we link to the main Pyrenan-Provençal collision phase. It is recognized in other U/Pb
441 age dataset from Provence (Zeboudj et al., 2025), and corresponds to a north-south compression
442 spanning from 59 to 34 Ma regarded as the culmination of the Pyrenean-Provençal collision
443 caused by plate-scale dynamic changes (Bestani et al., 2016; Balansa et al., 2022; Vacherat et
444 al., 2016; Moutherau et al., 2014; 2021) (Fig. 12B). In northwestern Europe, the Eocene also
445 heralds the onset of the West European Rift (WER), which was active until the Oligocene and
446 just precedes the opening of the Gulf of Lion (e.g. Séranne et al., 1999; Dèzes et al., 2004;
447 Moutherau et al., 2021).

448

449 **5.3 Oligocene rifting related to the West European Rift development (35-23 Ma)**

450 The WER stage is represented in our dataset by eight U/Pb dates ranging from 30.4 ± 2.7 to
451 24.3 ± 1.3 Ma associated with NW-SE to NE-SW extension (Fig. 12C). They coincide with the
452 extensional phase (35–23 Ma) documented in Provence, Western Alps, Eastern Pyrenees, and
453 Valencia Trough (Merle and Michon, 2001; Ziegler and Dèzes, 2006). The Late Eocene-Early
454 Oligocene period also coincides with the onset of the Alpine foreland (Ford et al., 1999). The
455 flexural bending of the European margin caused by Alpine loading likely increased extensional
456 stresses in the foreland, where the WER formed, however the available data are insufficient to
457 draw definitive conclusions. From Chattian-Aquitian times, at ca. 23 Ma, the opening of the
458 Gulf of Lion and of the Ligurian basin (e.g., Séranne et al., 1999; Jolivet et al., 1999, 2020)
459 initiated following the demise of the WER suggesting a tectonic relationship between these two
460 rifting events (Moutherau et al., 2021) (Fig. 12C). In our study area, the shallow depth of the
461 iso-velocity contour $V_s=4.2 \text{ km.s}^{-1}$, considered to be a proxy for the Moho (Schwartz et al.,
462 2024), and the 3D geological modelling (Bienveignant et al., 2024), confirms a significant
463 crustal thinning in the Valence-Rhône depression, where structures related to the WER are
464 preserved (Fig. S2, Supplementary Material 1). The excellent preservation of the Oligocene-
465 Miocene extensional phase in our dataset suggests a positive feedback between crustal thinning
466 (Fig. S2, Supplementary Material 1) and physical conditions that became favourable for calcite
467 precipitation at shallower depths, as the basin was progressively exhumed following Late
468 Cretaceous shortening.

469

470 **5.4 Alpine collision and fold and thrust belt propagation (<16 Ma)**

471 The youngest calcite U/Pb ages of 12.2 ± 3.2 Ma, 12.5 ± 5.2 Ma, 7.8 ± 0.6 Ma and 7.0 ± 2.2
472 Ma are associated with NE-SW compression. This result agrees with the westward propagation

473 of the Alpine deformation front, which migrated forelandward from 16 to 7 Ma in the Vercors
474 massif (Bilau et al., 2023a; Mai Yung Sen et al., 2025) to the north of the Vocontian Basin (Fig.
475 12D). This timing also coincides with the exhumation of Alpine basement, such as the
476 Belledonne and Pelvoux massifs, which accelerated at ca. 12 Ma (e.g. Beucher et al., 2012;
477 Girault et al., 2022; Boschetti et al., 2025a). This age range is also in agreement with the Digne
478 Nappe emplacement at 13-9 Ma (Schwartz et al., 2017) and fold and thrust development in the
479 frontal southern Alps between 18.2 ± 1.1 Ma and 3.16 ± 0.47 Ma obtained (Bauer et al., 2025 ;
480 Tigroudja et al., 2025).

481

482 CONCLUSION

483 The goal of this study was to provide a refined chronology of deformation in the Vocontian
484 Basin using an integrated approach combining U-Pb calcite geochronology, RSCM
485 thermometry, and subsidence analysis. First, this study highlights the absence of mid-
486 Cretaceous syn-rift calcites associated with the opening of the Vocontian Basin. This is possibly
487 related to dissolution during subsequent burial, or reflect the localization of fluid flow and strain
488 in the basal Triassic salt layer during the mid-Cretaceous extension. The temporal distribution
489 of dated brittle structures reveals three main deformation episodes: (1) Late Cretaceous to
490 Paleocene calcite precipitation associated with Pyrenean-Provençal convergence and diapirism;
491 (2) Oligocene extensional phases tied to the West European Rift opening; and (3) Miocene
492 strike-slip reactivation and contraction linked to the Alpine orogeny. These events are
493 superimposed onto a long-term subsidence history that records major burial phases during the
494 Jurassic and Cretaceous. Thermal data from RSCM analyses delineate a sharp eastward increase
495 in geothermal gradients, suggesting enhanced crustal thinning and/or diapiric activity in the
496 eastern part of the basin. This work highlights a good coherence of the local deformation
497 inferred from calcite U–Pb dating and paleostress analysis, and the regional tectonic evolution.

498

499 Declaration of Competing Interest

500 The authors declare that they have no known competing financial interests or personal
501 relationships that could have appeared to influence the work reported in this paper.

502

503 Availability of data material

504 The dataset(s) supporting the conclusions of this article is(are) available in Supplementary
505 Material 1.

506

507 **Acknowledgments**

508 Authors would like to thank BRGM and the RGF program which allows the founding this
509 project.

510

511 **Author's contribution**

512 LB is the corresponding author who carried out the field investigation, analysis, interpretation
513 and drafting of the manuscript. MP carried out the field investigations, analysis and review of
514 the manuscript. FM carried out the field investigation, interpretation, drafting a review of the
515 manuscript. GH carried out the U-Pb analysis and review of the Manuscript. SS and YR carried
516 out the field investigation and review of the manuscript. DB carried out interpretation and
517 discussion and AL carried out analysis of Raman data.

518 **Funding**

519 This study was made possible thanks to ministerial funding from the SDU2E doctoral school at
520 Toulouse University and by additional the funding by the RFG-Alps programme, coordinated
521 by the BRGM.

522

523 **References**

524 Allen, P. A., & Allen, J. R.: Basin analysis: Principles and application to petroleum play
525 assessment. John Wiley & Sons, 2013.

526 Angelier, J.: Inversion of field data in fault tectonics to obtain the regional stress—III.
527 A new rapid direct inversion method by analytical means. *Geophysical Journal
528 International*, 103(2), 363-376. <https://doi.org/10.1111/j.1365-246X.1990.tb01777.x>,
529 1990.

530 Angrand, P., & Mouthereau, F.: Evolution of the Alpine orogenic belts in the Western
531 Mediterranean region as resolved by the kinematics of the Europe-Africa diffuse plate
532 boundary. *BSGF-Earth Sciences Bulletin*, 192(1), 42.
533 <https://doi.org/10.1051/bsgf/2021031>, 2021.

534 Arnaud H., Charollais J., Delamette M. & Portault B. : Crétacé supérieur. Chaînes
535 subalpines. In: S. Debrand-Passard et al., Eds, *Syn thèse géo lo gique du Sud-Est de la*
536 *France. – Mém.BRGM*, 125, 355-359, 1984.

537 Balansa, J., Espurt, N., Hippolyte, J. C., Philip, J., & Caritg, S.: Structural evolution of
538 the superimposed Provençal and Subalpine fold-thrust belts (SE France). *Earth-Science
539 Reviews*, 227, 103972. <https://doi.org/10.1016/j.earscirev.2022.103972>, 2022.

540 Balansa, J., Lahfid, A., Espurt, N., Hippolyte, J. C., Henry, P., Caritg, S., & Fasentieux, B.:
541 Unraveling the eroded units of mountain belts using RSCM thermometry and cross-
542 section balancing: example of the southwestern French Alps. *International Journal of*
543 *Earth Sciences*, 112(2), 443-458. <https://doi.org/10.1007/s00531-022-02257-3>, 2023.

544 Bauer, R., Corsini, M., Matonti, C., Bosch, D., Bruguier, O., & Issautier, B.: The role of
545 Cretaceous tectonics in the present-day architecture of the Nice arc (Western Subalpine
546 foreland, France). *Journal of Structural Geology*, 105538, 2025.

547 Bestani, L., Espurt, N., Lamarche, J., Bellier, O., & Hollender, F.: Reconstruction of the
548 Provence Chain evolution, southeastern France. *Tectonics*, 35(6), 1506-1525-
549 <https://doi.org/10.1002/2016TC004115>, 2016.

550 Beaudoin, B., Friès, G., Joseph, P., Bouchet, R., & Cabrol, C. : Tectonique
551 synsédimentaire crétacée à l'ouest de la Durance (S.-E. France). *Comptes rendus de*
552 *l'Académie des sciences. Série 2, Mécanique, Physique, Chimie, Sciences de l'univers,*
553 *Sciences de la Terre*, 303(8), 713-718, 1986.

554 Beucher, R., van der Beek, P., Braun, J., & Batt, G. E.: Exhumation and relief
555 development in the Pelvoux and Dora-Maira massifs (Western Alps) assessed by
556 spectral analysis and inversion of thermochronological age transects. *Journal of*
557 *Geophysical Research: Earth Surface*, 117(F3). <https://doi.org/10.1029/2011JF002240>,
558 2012.

559 Bièvre, G., & Quesne, D.: Synsedimentary collapse on a carbonate platform margin μ
560 (lower Barremian, southern Vercors, SE France). *Geodiversitas*, 26(2), 169-184, 2004.

561 Bienveignant, D., Nouibat, A., Sue, C., Rolland, Y., Schwartz, S., Bernet, M., Dumont, T.,
562 Nomade, J., Caritg, S., & Walpersdorf, A.: Shaping the crustal structure of the SW-
563 Alpine Foreland : Insight from 3D modeling. *Tectonophysics*, 889, 230471.
564 <https://doi.org/10.1016/j.tecto.2024.230471>, 2024.

565 Bilau, A., Bienveignant, D., Rolland, Y., Schwartz, S., Godeau, N., Guihou, A., et al.: The
566 Tertiary structuration of the Western Subalpine foreland deciphered by calcite-filled
567 faults and veins. *Earth Science Reviews*, 236, 104270, 2023a.

568 Bilau, A., Rolland, Y., Dumont, T., Schwartz, S., Godeau, N., Guihou, A., & Deschamps, P.,
569 2023b. Early onset of Pyrenean collision (97–90 Ma) evidenced by U–Pb dating on
570 calcite (Provence, SE France). *Terra Nova*, 35(5), 413-423.
571 <https://doi.org/10.1111/ter.12665>, 2004

572 Boschetti, L., Schwartz, S., Rolland, Y., Dumont, T., and Nouibat, A.: A new tomographic-
573 petrological model for the Ligurian-Provence back-arc basin (North-Western

574 Mediterranean Sea), Tectonophysics, 230111,
575 <https://doi.org/10.1016/j.tecto.2023.230111>, 2023.

576 Boschetti, L., Mouthereau, F., Schwartz, S., Rolland, Y., Bernet, M., Balvay, M., ... & Lahfid,
577 A.: Thermochronology of the western Alps (Pelvoux massif) reveals the longterm
578 multiphase tectonic history of the European paleomargin. Tectonics, 44(2),
579 e2024TC008498. <https://doi.org/10.1029/2024TC008498>, 2025a.

580 Boschetti, L., Rolland, Y., Mouthereau, F., Schwartz, S., Milesi, G., Munch, P., Bernet, M.,
581 Balvay, M., Thiéblemont, D., Bonno, M., Martin, C., and Monié, P.: Thermochronology
582 of the Maures-Tanneron crystalline basement: insights for SW Europe Triassic to
583 Miocene tectonic history, Swiss J. Geosci., 118, 14, <https://doi.org/10.1186/s00015-025-00485-8>, 2025b.

585 Boschetti, L., Boulle, C., Rolland, Y., Schwartz, S., Milesi, G., Bienveignant, D., et al. Shear
586 zone memory revealed by in-situ Rb-Sr and 40Ar/39Ar dating of Pyrenean and Alpine
587 tectonic phases in the external Alps. *Lithos*, 108168, 2025c.

588 Célini, N. : Le rôle des évaporites dans l'évolution tectonique du front alpin: le cas de la
589 nappe de Digne (Doctoral dissertation, Université de Pau et des Pays de l'Adour), 2020.

590 Célini, N., Mouthereau, F., Lahfid, A., Gout, C., and Callot, J.-P.: Rift thermal inheritance in
591 the SW Alps (France): insights from RSCM thermometry and 1D thermal numerical
592 modelling, Solid Earth, 14, 1–16, <https://doi.org/10.5194/se-14-1-2023>, 2023.

593 Célini, N., Pichat, A., Mouthereau, F., Ringenbach, J. C., & Callot, J. P.: Along-strike
594 variations of structural style in the external Western Alps (France): Review, insights
595 from analogue models and the role of salt. Journal of Structural Geology, 179, 105048.
596 <https://doi.org/10.1016/j.jsq.2023.105048>, 2024.

597 Chanvry, E., Marchand, E., Lopez, M., Séranne, M., Le Saout, G., & Vinches, M. :
598 Tectonic and climate control on allochthonous bauxite deposition. Example from the
599 mid-Cretaceous Villeveyrac basin, southern France. Sedimentary Geology, 407,
600 105727. <https://doi.org/10.1016/j.sedgeo.2020.105727>, 2020.

601 Combes, P. J. : Typologie, cadre géodynamique et genèse des bauxites françaises.
602 Geodinamica Acta, 4(2), 91-109. <https://doi.org/10.1080/09853111.1990.11105202>,
603 1990.

604 Cotillon, P., Ferry, S., Busnardo, R., Lafarge, D., & Renaud, B.: Synthèse
605 stratigraphique et paléogéographique sur les faciès urgoniens du Sud de l'Ardèche et du
606 Nord du Gard (France SE). Geobios, 12, 121-139. [https://doi.org/10.1016/S0016-6995\(79\)80055-8](https://doi.org/10.1016/S0016-6995(79)80055-8), 1979.

608 Dall'Asta, N., Hoareau, G., Manatschal, G., Centrella, S., Denèle, Y., Ribes, C., & Kalifi, A. :
609 Structural and petrological characteristics of a Jurassic detachment fault from the Mont-
610 Blanc massif (Col du Bonhomme area, France). *Journal of Structural Geology*, 159,
611 104593. <https://doi.org/10.1016/j.jsg.2022.104593>, 2022.

612 Dardeau, G., Atrops, F., Fortwengler, D., De Graciansky, P. C., & Marchand, D. : Jeux
613 de blocs et tectonique distensive au Callovien et à l'Oxfordien dans le bassin du Sud-Est
614 de la France. *Bulletin de la Société géologique de France*, 4(5), 771-777, 1988.

615 Debèlmas, J. : La zone subbriançonnaise et la zone valaisanne savoyarde dans le cadre
616 de la tectonique des plaques. *Géologie Alpine*, 77, 3-8, 1988, 2001.

617 Delvaux, D., & Sperner, B.: New aspects of tectonic stress inversion with reference to
618 the TENSOR program. <https://doi.org/10.1144/GSL.SP.2003.212.01.06>, 2003.

619 Debrand-Passard, S. : *Synthèse géologique du Sud-Est de la France* (Vol. 1).
620 Editions BRGM.de Graciansky, P.C., & Lemoine, Marcel., 1988. Early Cretaceous
621 extensional tectonics in the southwestern French Alps; a consequence of North-
622 Atlantic rifting during Tethyan spreading. *Bulletin de la Société géologique de France*,
623 4(5), 733-737, 1984.

624 Dèzes, P., Schmid, S. M., & Ziegler, P. A. : Evolution of the European Cenozoic Rift
625 System: interaction of the Alpine and Pyrenean orogens with their foreland lithosphere.
626 *Tectonophysics*, 389(1-2), 1-33. <https://doi.org/10.1016/j.tecto.2004.06.011>, 2004.

627 Donard, A., Pottin, A. C., Pointurier, F., & Pécheyran, C.: Determination of relative rare
628 earth element distributions in very small quantities of uranium ore concentrates using
629 femtosecond UV laser ablation-SF-ICP-MS coupling. *Journal of Analytical Atomic
630 Spectrometry*, 30(12), 2420-2428, 2015.

631 Espurt, N., Angrand, P., Teixell, A., Labaume, P., Ford, M., de Saint Blanquat, M., & Chevrot,
632 S. Crustal-scale balanced cross-section and restorations of the Central Pyrenean belt
633 (Nestes-Cinca transect): Highlighting the structural control of Variscan belt and
634 Permian-Mesozoic rift systems on mountain building. *Tectonophysics*, 764, 25-45.
635 <https://doi.org/10.1016/j.tecto.2019.04.026>, 2019.

636 Flandrin, J. : Sur l'âge des principaux traits structuraux du Diois et des Baronnies.
637 *Bulletin de la Société géologique de France*, 7(3), 376-386.
638 <https://doi.org/10.2113/gssgbull.S7-VIII.3.376>, 1966.

639 Ford, M., Lickorish, W.H. & Kusznir, N.J.: Tertiary foreland sedimentation in the
640 southern Subalpine chains, SE France: a geodynamic analysis. *Basin Research*, 11, 315–
641 336. <https://doi.org/10.1046/j.1365-2117.1999.00103.x>, 1999

642 Ford, M., & Lickorish, W. H.: Foreland basin evolution around the western Alpine Arc.
643 <https://doi.org/10.1144/GSL.SP.2004.221.01.04>, 2004.

644 Ford, M., Masini, E., Vergés, J., Pik, R., Ternois, S., Léger, J., ... & Calassou, S.:
645 Evolution of a low convergence collisional orogen: a review of Pyrenean orogenesis.
646 BSGF-Earth Sciences Bulletin, 193(1), 19. <https://doi.org/10.1051/bsgf/2022018>, 2022.

647 Gidon, M., Arnaud, H., Pairis, J. L., AprAHAMIAN, J., & Uselle, J. P. : Les
648 déformations tectoniques superposées du Dévoluy méridional (Hautes-Alpes). Géologie
649 Alpine, 46, 87-110, 1970.

650 Girault, J. B., Bellahsen, N., Bernet, M., Pik, R., Loget, N., Lasseur, E., ... & Sonnet, M.:
651 Exhumation of the Western Alpine collisional wedge: New thermochronological data.
652 Tectonophysics, 822, 229155. <https://doi.org/10.1016/j.tecto.2021.229155>, 2022.

653 Guilhaumou, N., Touray, J. C., Perthuisot, V., & Roure, F., Palaeocirculation in the
654 basin of southeastern France sub-alpine range: a synthesis from fluid inclusions studies.
655 Marine and Petroleum Geology, 13(6), 695-706. [https://doi.org/10.1016/0264-8172\(95\)00064-X](https://doi.org/10.1016/0264-8172(95)00064-X). 1996.

656 Guyonnet-Benaize, C., Lamarche, J., Masse, J. P., Villeneuve, M., & Viseur, S. : 3D
657 structural modelling of small-deformations in poly-phase faults pattern. Application to
658 the Mid-Cretaceous Durance uplift, Provence (SE France). Journal of Geodynamics,
659 50(2), 81-93. <https://doi.org/10.1016/j.jog.2010.03.003>, 2010.

660 Hoareau, G., Claverie, F., Pecheyran, C., Barbotin, G., Perk, M., Beaudoin, N. E., ... & Rasbury,
661 E. T.: The virtual spot approach: a simple method for image U-Pb carbonate
662 geochronology by high-repetition rate LA-ICP-MS. EGUsphere, 2024, 1-35.
663 <https://doi.org/10.5194/egusphere-2024-2366>, 2024.

664 Hoareau, G., Claverie, F., Pecheyran, C., Paroissin, C., Grignard, P. A., Motte, G., ... & Girard,
665 J. P.: Direct U–Pb dating of carbonates from micron-scale femtosecond laser ablation
666 inductively coupled plasma mass spectrometry images using robust regression.
667 Geochronology, 3(1), 67-87. <https://doi.org/10.5194/gchron-3-67-2021>, 2021.

668 Homberg, C., Barrier, E., Mroueh, M., Muller, C., Hamdan, W., & Higazi, F.: Tectonic
669 evolution of the central Levant domain (Lebanon) since Mesozoic time.
670 <https://doi.org/10.1144/SP341.12>, 2010.

671 Homberg, C., Schnyder, J., & Benzaggagh, M.: Late Jurassic-Early Cretaceous faulting
672 in the Southeastern French Basin: does it reflect a tectonic reorganization?. Bulletin de
673 la Société géologique de France, 184(4-5), 501-514.
674 <https://doi.org/10.2113/gssgbull.184.4-5.501>, 2013.

676 Hippolyte, J. C., Angelier, J., Bergerat, F., Nury, D., & Guieu, G.: Tectonic-stratigraphic
677 record of paleostress time changes in the Oligocene basins of the Provence, southern
678 France. *Tectonophysics*, 226(1-4), 15-35. [https://doi.org/10.1016/0040-1951\(93\)90108-V](https://doi.org/10.1016/0040-1951(93)90108-V). 1993

680 Huang, Q., Geometry and tectonic significance of Albian sedimentary dykes in the Sisteron
681 area, SE France, *J. Struct. Geol.*, 10, 453–462, 1988.

682 Jolivet, L., Frizon de Lamotte, D., Mascle, A., & Séranne, M.: The Mediterranean
683 basins: Tertiary extension within the Alpine orogen—An introduction. *Geological
684 Society, London, Special Publications*, 156(1), 1-14.
685 <https://doi.org/10.1144/GSL.SP.1999.156.01.02>, 1999

686 Jolivet, L., Menant, A., Roche, V., Le Pourhiet, L., Maillard, A., Augier, R., ... & Canva, A.:
687 Transfer zones in Mediterranean back-arc regions and tear faults. *Bulletin de la Société
688 Géologique de France*, 192(1). <https://doi.org/10.1051/bsgf/2021006>, 2021.

689 Joseph, P., Beaudoin, B., Sempere, T., & Maillart, J. : Vallées sous-marines et systèmes
690 d'épandages carbonatés du Berriasien vocontien (Alpes méridionales françaises). *Bull.
691 Soc. Geol. Fr*, 8, 363-374, 1988.

692 Kouketsu, Y., Mizukami, T., Mori, H., Endo, S., Aoya, M., Hara, H., ... & Wallis, S.: A
693 new approach to develop the Raman carbonaceous material geothermometer for low-
694 grade metamorphism using peak width. *Island Arc*, 23(1), 33-50.
695 <https://doi.org/10.1111/iar.12057>, 2014.

696 Lacombe, O., Beaudoin, N. E., Hoareau, G., Labeur, A., Pecheyran, C., and Callot, J.-P.: Dating
697 folding beyond folding, from layer-parallel shortening to fold tightening, using
698 mesostructures: lessons from the Apennines, Pyrenees, and Rocky Mountains, *Solid
699 Earth*, 12, 2145–2157, <https://doi.org/10.5194/se-12-2145-2021>, 2021.

700 Lahfid, A., Beyssac, O., Deville, E., Negro, F., Chopin, C., & Goffé, B. (2010). Evolution of
701 the Raman spectrum of carbonaceous material in low-grade metasediments of the Glarus
702 Alps (Switzerland). *Terra nova*, 22(5), 354-360. <https://doi.org/10.1111/j.1365-3121.2010.00956.x>, 2010.

704 Le Breton, E., Brune, S., Ustaszewski, K., Zahirovic, S., Seton, M., & Müller, R. D. :
705 Kinematics and extent of the Piemont–Liguria Basin—implications for subduction
706 processes in the Alps. *Solid Earth*, 12(4), 885-913. <https://doi.org/10.5194/se-12-885-2021>, 2021.

708 Lemoine, M. : Rythme et modalités des plissements superposés dans les chaînes

709 subalpines méridionales des Alpes occidentales françaises. *Geologische Rundschau*, 61,
710 975-1010. <https://doi.org/10.1007/BF01820902>, 1972.

711 Lemoine, M., Bas, T., Arnaud-Vanneau, A., Arnaud, H., Dumont, T., Gidon, M., Bourbon, M.,
712 Graciansky, P.-C. de, Rudkiewicz, J.-L., Megard-Galli, J., and Tricart, P.: The
713 continental margin of the Mesozoic Tethys in the Western Alps, *Mar Petrol Geol*, 3,
714 179–199, [https://doi.org/10.1016/0264-8172\(86\)90044-9](https://doi.org/10.1016/0264-8172(86)90044-9), 1986.

715 Lemoine, M., Tricart, P. and Boillot, G.: Ultramafic and gabbroic ocean floor of the
716 Ligurian Tethys (Alps, Corsica, Apennines): in search for a genetic model. *Geology*, 15:
717 622-625, 1987.

718 Manatschal, G., & Müntener, O.: A type sequence across an ancient magma-poor ocean–
719 continent transition: the example of the western Alpine Tethys ophiolites.
720 *Tectonophysics*, 473(1-2), 4-19. <https://doi.org/10.1016/j.tecto.2008.07.021>, 2009

721 Marchand, E., Séranne, M., Bruguier, O., & Vinches, M. : LA-ICP-MS dating of detrital
722 zircon grains from the Cretaceous allochthonous bauxites of Languedoc (south of
723 France): Provenance and geodynamic consequences. *Basin Research*, 33(1), 270-290.
724 <https://doi.org/10.1111/bre.12465>, 2021.

725 Merle, O., & Michon, L.: The formation of the West European Rift; a new model as
726 exemplified by the Massif Central area. *Bulletin de la Société géologique de France*,
727 172(2), 213-221. <https://doi.org/10.2113/172.2.213>, 2021.

728 Mohn, G., Manatschal, G., Beltrando, M., & Haupert, I.: The role of rift-inherited hyper-
729 extension in Alpine-type orogens. *Terra Nova*, 26(5), 347-353.
730 <https://doi.org/10.1111/ter.12104>, 2014.

731 Montenat, C., Janin, M. C., & Barrier, P. : L'accident du Toulourenc: une limite
732 Tectonique entre la plate-forme provençale et le Bassin vocontien à l'Aptien–Albien (SE
733 France). *Comptes rendus. Géoscience*, 336(14), 1301-1310, 2004.

734 Moutheraeau, F., Filleaudeau, P. Y., Vacherat, A., Pik, R., Lacombe, O., Fellin, M. G., ... &
735 Masini, E.: Placing limits to shortening evolution in the Pyrenees: Role of margin
736 architecture and implications for the Iberia/Europe convergence. *Tectonics*, 33(12),
737 2283-2314. <https://doi.org/10.1002/2014TC003663>, 2014.

738 Moutheraeau, F., Angrand, P., Jourdon, A., Ternois, S., Fillon, C., Calassou, S., ... & Baudin, T.:
739 Cenozoic mountain building and topographic evolution in Western Europe: impact of
740 billions of years of lithosphere evolution and plate kinematics. *BSGF-Earth Sciences*
741 *Bulletin*, 192(1), 56. <https://doi.org/10.1051/bsgf/2021040>, 2021.

742 Muñoz, J. A.: Evolution of a continental collision belt: ECORS-Pyrenees crustal

743 balanced cross-section. In *Thrust tectonics* (pp. 235-246). Dordrecht: Springer
744 Netherlands, 1992.

745 Olivetti, V., Godard, V., Bellier, O., & Aster Team.: Cenozoic rejuvenation events of
746 Massif Central topography (France): Insights from cosmogenic denudation rates and
747 river profiles. *Earth and Planetary Science Letters*, 444, 179-191.
748 <https://doi.org/10.1016/j.epsl.2016.03.049>, 2016.

749 Parizot, O., Missenard, Y., Haurine, F., Blaise, T., Barbarand, J., Benedicto, A., & Sarda, P.:
750 When did the Pyrenean shortening end? Insight from U-Pb geochronology of syn-
751 faulting calcite (Corbières area, France). *Terra nova*, 33(6), 551-559.
752 <https://doi.org/10.1111/ter.12547>, 2021.

753 Parizot, O., Missenard, Y., Barbarand, J., Blaise, T., Benedicto, A., Haurine, F., & Sarda, P.:
754 How sensitive are intraplate inherited structures? Insight from the Cévennes Fault
755 System (Languedoc, SE France). *Geological Magazine*, 159(11-12), 2082-2094.
756 <https://doi.org/10.1017/S0016756822000152>, 2022.

757 Ribes, C., Ghienne, J. F., Manatschal, G., Dall'Asta, N., Stockli, D. F., Galster, F., ... & Karner,
758 G. D.: The Grès Singuliers of the Mont Blanc region (France and Switzerland):
759 stratigraphic response to rifting and crustal necking in the Alpine Tethys. *International
760 Journal of Earth Sciences*, 109, 2325-2352. <https://doi.org/10.1007/s00531-020-01902-z>, 2020.

761
762 Roure, F., Brun, J. P., Colletta, B., & Van Den Driessche, J.: Geometry and kinematics
763 of extensional structures in the Alpine foreland basin of southeastern France. *Journal of
764 Structural Geology*, 14(5), 503-519. [https://doi.org/10.1016/0191-8141\(92\)90153-N](https://doi.org/10.1016/0191-8141(92)90153-N),
765 1992.

766 Saspiturry, N., Lahfid, A., Baudin, T., Guillou-Frottier, L., Razin, P., Issautier, B., ... & Corre,
767 B.: Paleogeothermal gradients across an inverted hyperextended rift system: Example
768 of the Mauléon Fossil Rift (Western Pyrenees). *Tectonics*, 39(10), e2020TC006206.
769 <https://doi.org/10.1029/2020TC006206>, 2020.

770 Schito, A., Romano, C., Corrado, S., Grigo, D., & Poe, B.: Diagenetic thermal evolution
771 of organic matter by Raman spectroscopy. *Organic Geochemistry*, 106, 57-67.
772 <https://doi.org/10.1016/j.orggeochem.2016.12.006>, 2017.

773 Schwartz, S., Gautheron, C., Audin, L., Dumont, T., Nomade, J., Barbarand, J., ... & van der
774 Beek, P.: Foreland exhumation controlled by crustal thickening in the Western Alps.
775 *Geology*, 45(2), 139-142, 2017

776 Schwartz, S., Rolland, Y., Nouibat, A., Boschetti, L., Bienveignant, D., Dumont, T., ... &

777 Moutherneau, F.: Role of mantle indentation in collisional deformation evidenced by
778 deep geophysical imaging of Western Alps. *Communications Earth & Environment*,
779 5(1), 17. <https://doi.org/10.1038/s43247-023-01180-y>, 2024.

780 Séranne, M.: The Gulf of Lion continental margin (NW Mediterranean) revisited by
781 IBS: an overview. *Geological Society, London, Special Publications*, 156(1), 15-36.
782 <https://doi.org/10.1144/GSL.SP.1999.156.01.03>, 1999.

783 Séranne, M., Couëffé, R., Husson, E., Baral, C., & Villard, J. : The transition from
784 Pyrenean shortening to Gulf of Lion rifting in Languedoc (South France)—A tectonic-
785 sedimentation analysis. *BSGF-Earth Sciences Bulletin*, 192(1), 27, 2021.

786 Simon-Labric, T., Rolland, Y., Dumont, T., Heymes, T., Authemayou, C., Corsini, M., and
787 Fornari, M.: 40Ar/39Ar dating of Penninic Front tectonic displacement (W Alps) during
788 the Lower Oligocene (31–34 Ma), *Terra Nova*, 21, 127–136,
789 <https://doi.org/10.1111/j.1365-3121.2009.00865.x>, 2009.

790 Teixell, A., Labaume, P., Ayarza, P., Espurt, N., de Saint Blanquat, M., & Lagabrielle, Y.:
791 Crustal structure and evolution of the Pyrenean-Cantabrian belt: A review and new
792 interpretations from recent concepts and data. *Tectonophysics*, 724, 146-170.
793 <https://doi.org/10.1016/j.tecto.2018.01.009>, 2018.

794 Tigroudja, L., Espurt, N., & Scalabrino, B.: Quantifying Miocene thin-and thick-skinned
795 shortening in the Baous thrust system, SW French Alpine Front. *Tectonophysics*,
796 230930, 2025.

797 Trümpy, R.: A possible Jurassic-Cretaceous transform system in the Alps and the
798 Carpathians. <https://doi.org/10.1130/SPE218-p93>, 1988.

799 Turco, E., Macchiavelli, C., Mazzoli, S., Schettino, A., & Pierantoni, P. P. : Kinematic
800 evolution of Alpine Corsica in the framework of Mediterranean mountain belts.
801 *Tectonophysics*, 579, 193-206, 2012.

802 Vacherat, A., Moutherneau, F., Pik, R., Bellahsen, N., Gautheron, C., Bernet, M., Daudet, M.,
803 Balansa, J., Tibari, B., Jamme, R. P., and Radal, J.: Rift-to-collision transition recorded
804 by tectonothermal evolution of the northern Pyrenees, *Tectonics*, 35, 907–933,
805 <https://doi.org/10.1002/2015tc004016>, 2016.

806 Wicker, V., & Ford, M.: Assessment of the tectonic role of the Triassic evaporites in the
807 North Toulon fold-thrust belt. *BSGF-Earth Sciences Bulletin*, 192(1), 51.
808 <https://doi.org/10.1051/bsgf/2021033>, 2021.

809 Zeboudj, A., Lacombe, O., Beaudoin, N. E., Callot, J. P., Lamarche, J., Guihou, A., & Hoareau,

810 G.: Sequence, duration, rate of deformation and paleostress evolution during fold
811 development: Insights from fractures, calcite twins and U-Pb calcite geochronology in
812 the Mirabeau anticline (SE France). *Journal of Structural Geology*, 105460.
813 <https://doi.org/10.1016/j.jsg.2025.105460>, 2025.

814 Ziegler, P. A., & Dèzes, P.: Crustal evolution of western and central Europe.
815 <https://doi.org/10.1144/GSL.MEM.2006.032.01.03>, 2006.

816

817

818

819

820

821

822

823

824

825

826

827

828

829

830

831

832

833

834

835

836

837

838

839

840

841

842

843

844

845

846

847

848

849

850

851

852

853

854

855

856

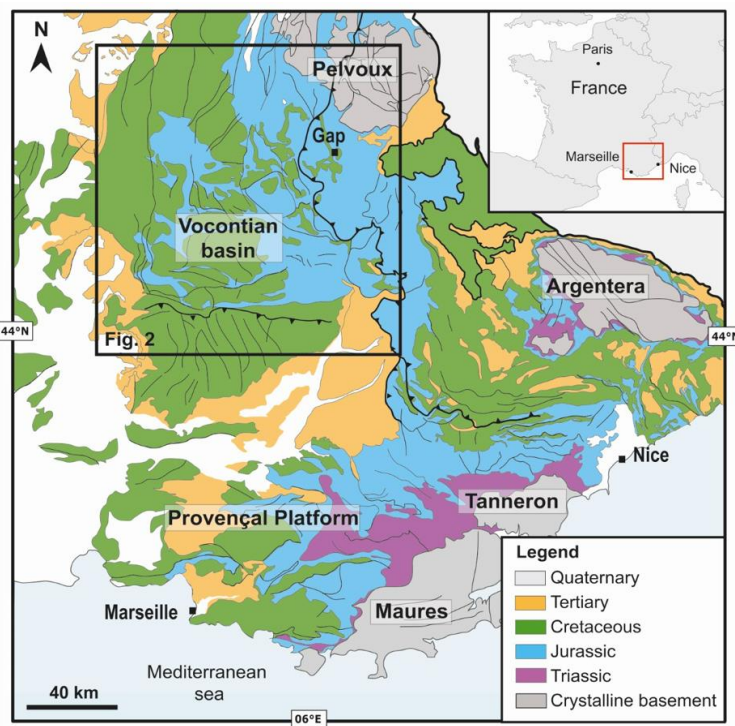


Figure 1: Simplified geological map of SE France. Location of the study area.

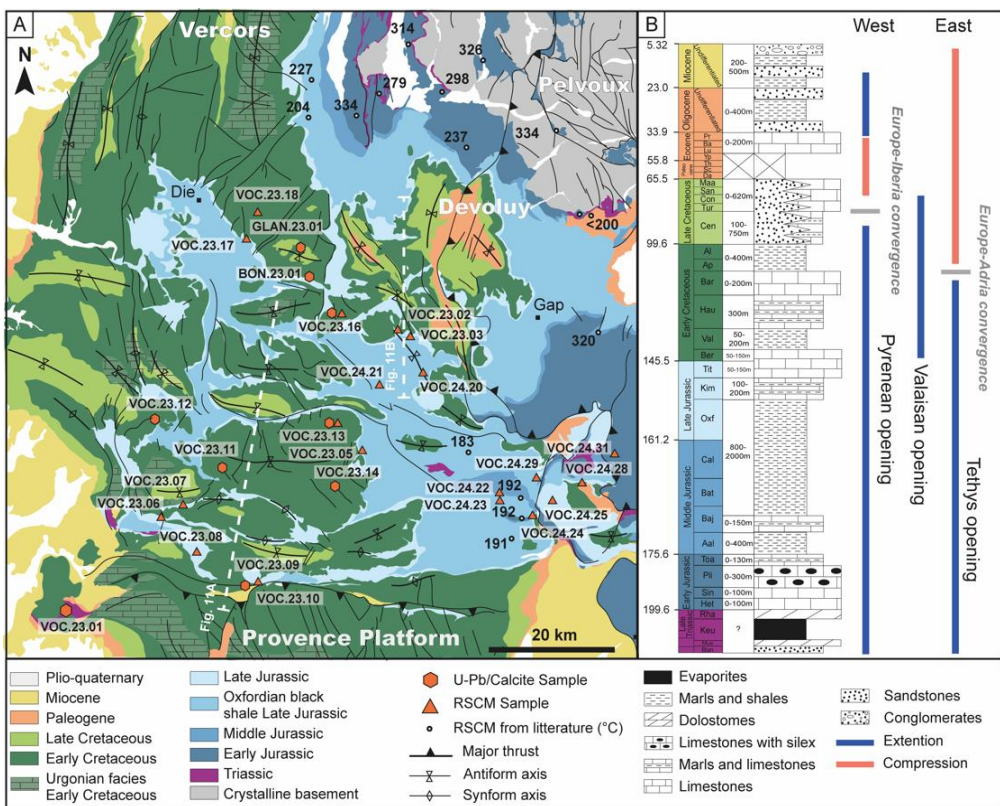


Figure 2: A) Geological map of Vocontian basin with sample location and Raman data in °C from Bellanger et al. (2015) and Céline et al. (2023). B) General stratigraphic section of the Vocontian basin and main tectonic events.

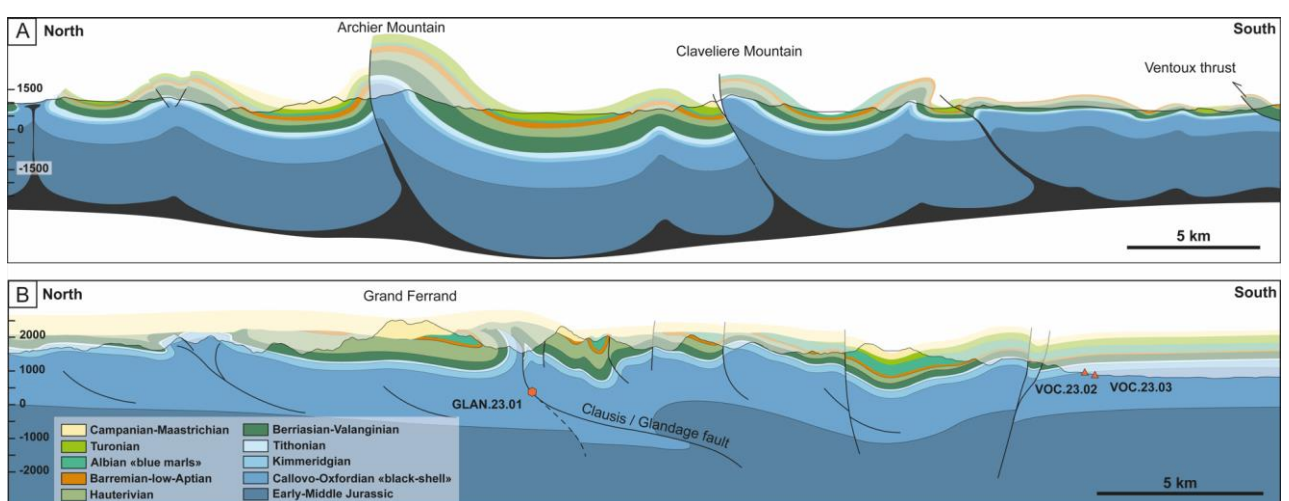


Figure 3: North-South geological cross-section of the Vocontian basin (A) and the Dévoluy massif (B). Location is presented in Fig. 2. Coniacian and Santonian are missing as there is a sedimentary gap (see in the text).

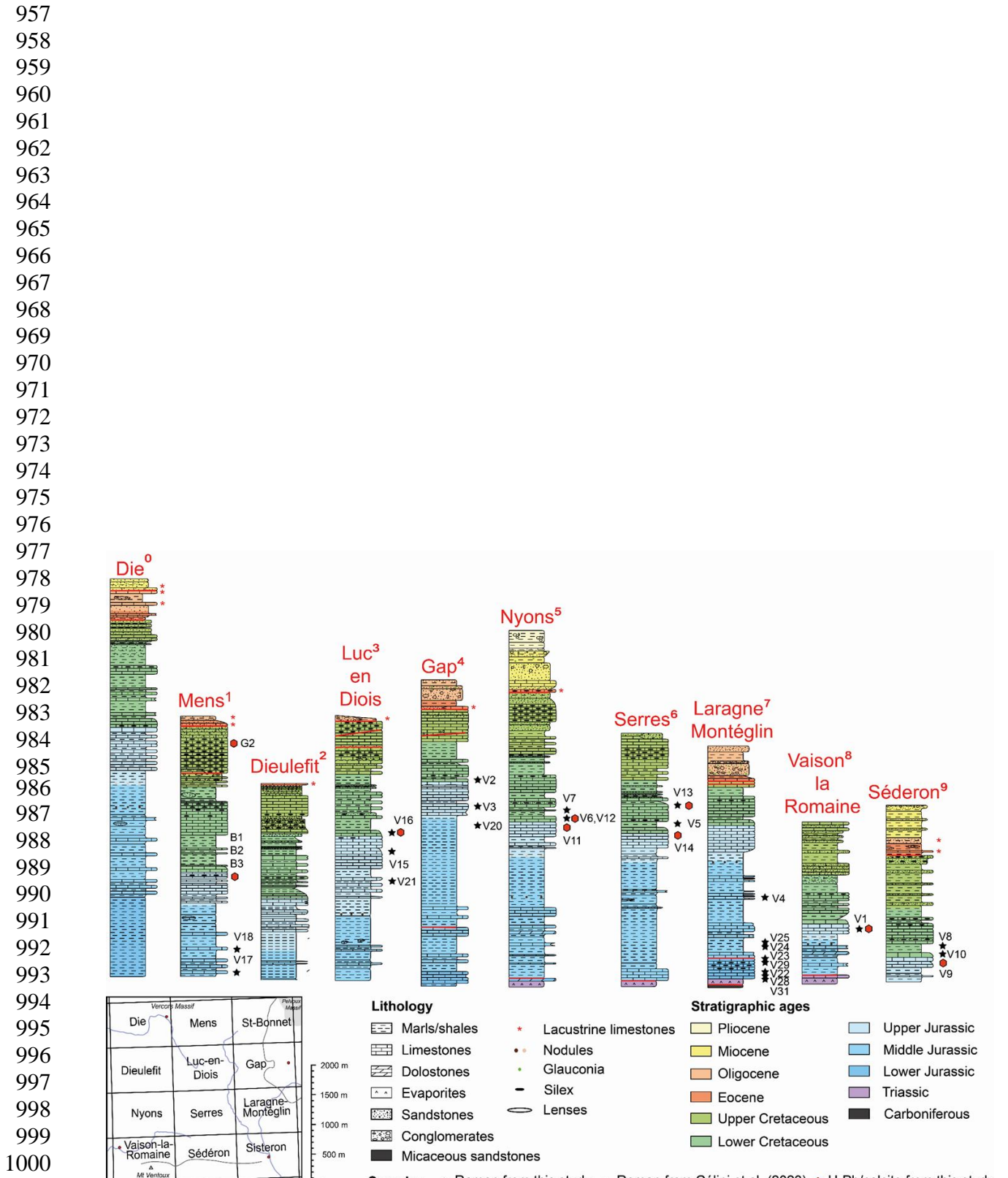


Figure 4: Stratigraphic logs corresponding to each geological notice of BRGM maps from the Vocontian basin. Sample names are shortened from V.23.X to VX for simplification and space in the figure.

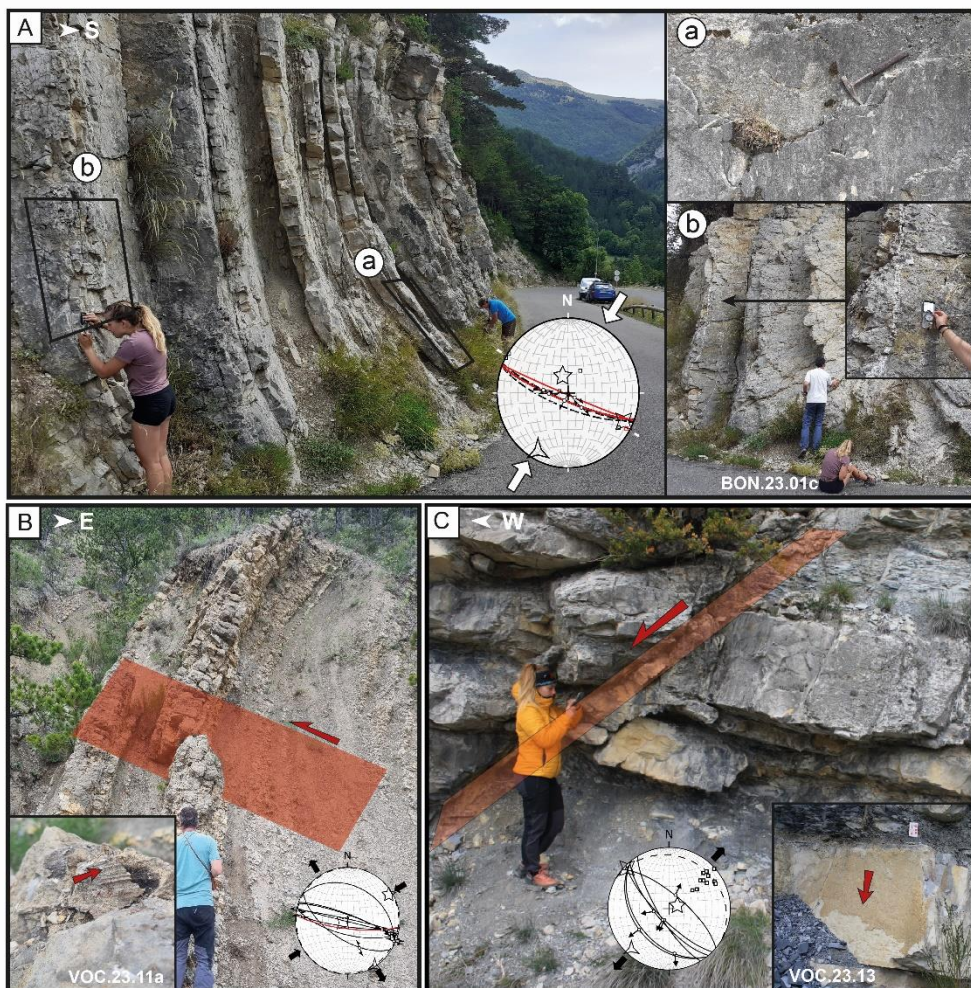


Figure 5: Main geological structures associated to their corresponding measurement and U-Pb age. A) sample BON.23.01. B) sample VOC.23.11. C) sample VOC.23.13.

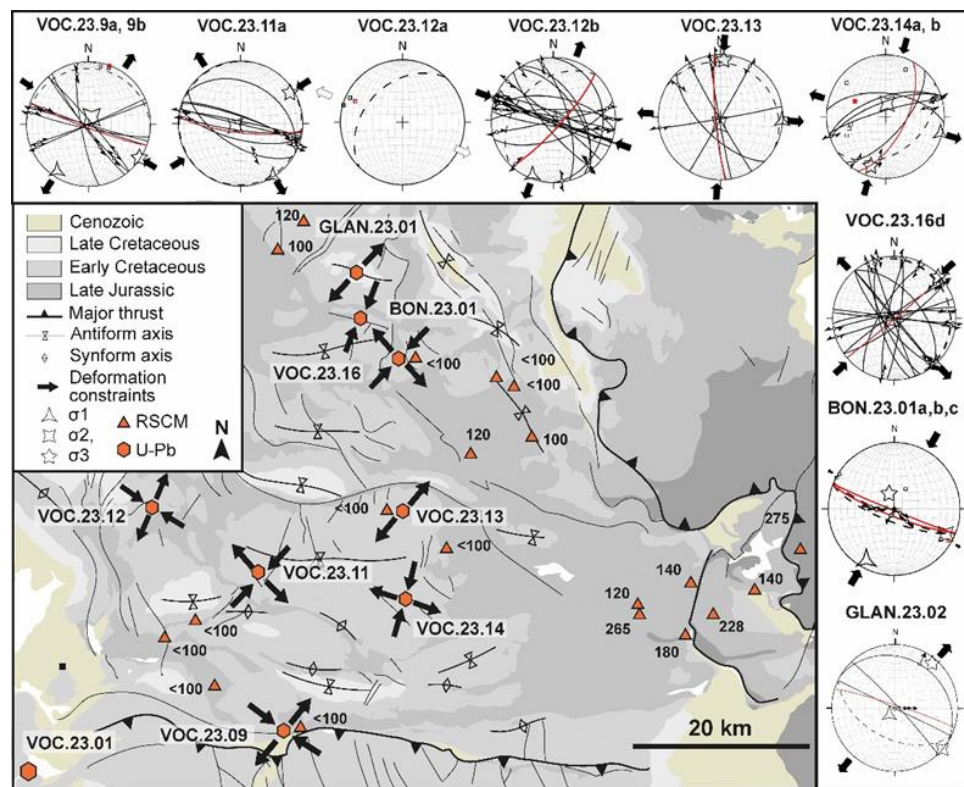


Figure 6: Simplified geological map with structural analysis of each dated sample and location of Raman thermometry results given in °C.

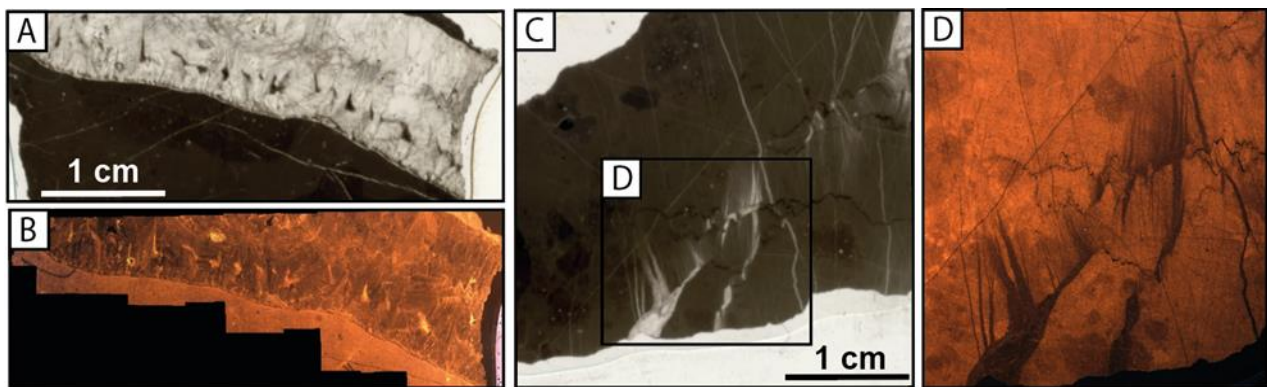


Figure 7: Examples of LPNA (A and C) and cathodoluminescence microphotographs (B and D) of two different types of U/Pb-dated calcite veins. A) and B) sample VOC-23-01. C) and D) sample VOC-23-11a.

1105
1106
1107
1108
1109
1110
1111
1112
1113
1114
1115
1116
1117
1118
1119
1120
1121
1122
1123
1124
1125
1126
1127
1128
1129
1130
1131
1132
1133
1134
1135
1136
1137
1138
1139
1140
1141
1142
1143
1144
1145
1146
1147
1148
1149
1150
1151
1152
1153
1154

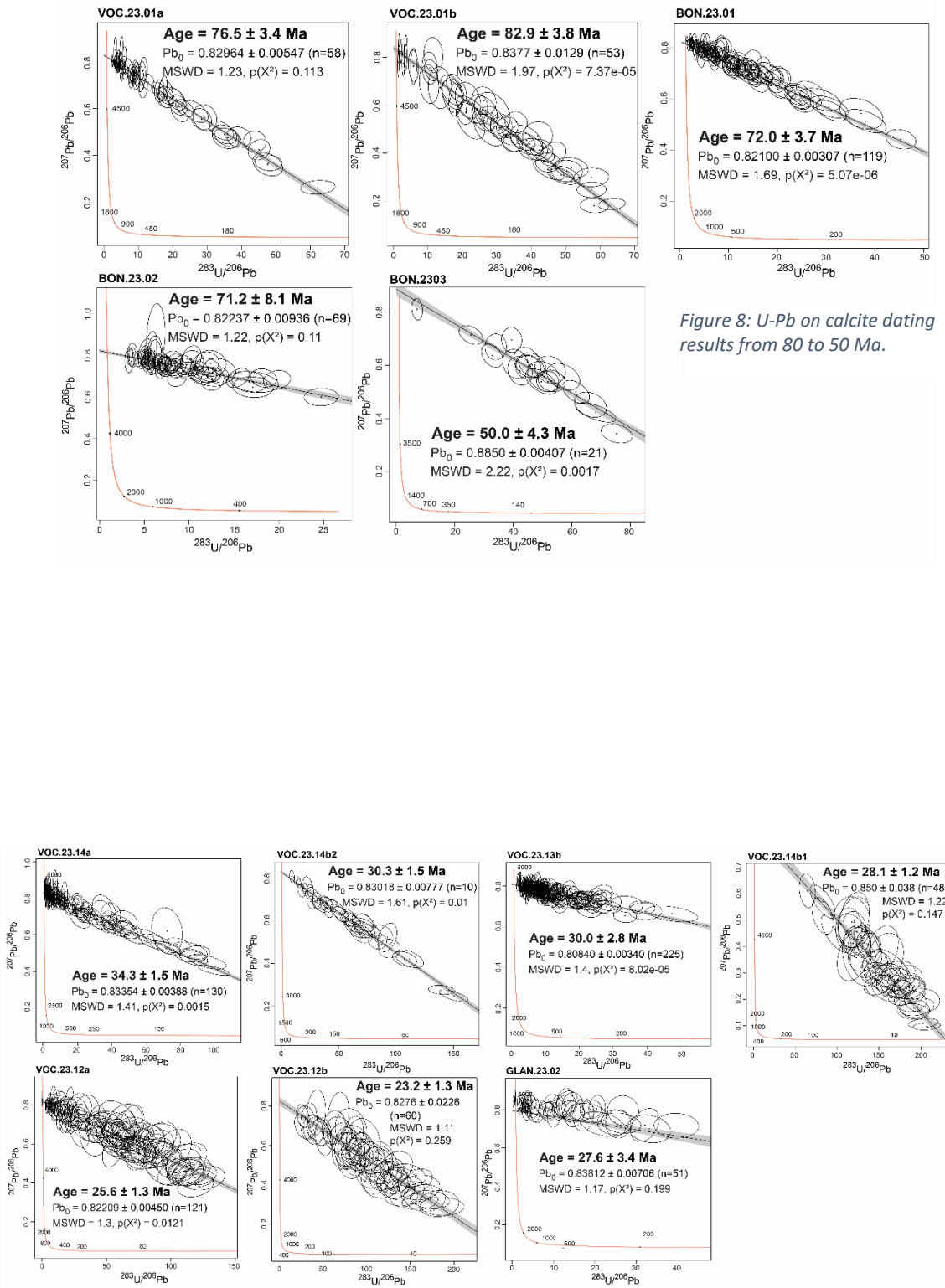


Figure 8: U-Pb on calcite dating results from 80 to 50 Ma.

Figure 9: U-Pb on calcite dating results from 30 to 20 Ma.

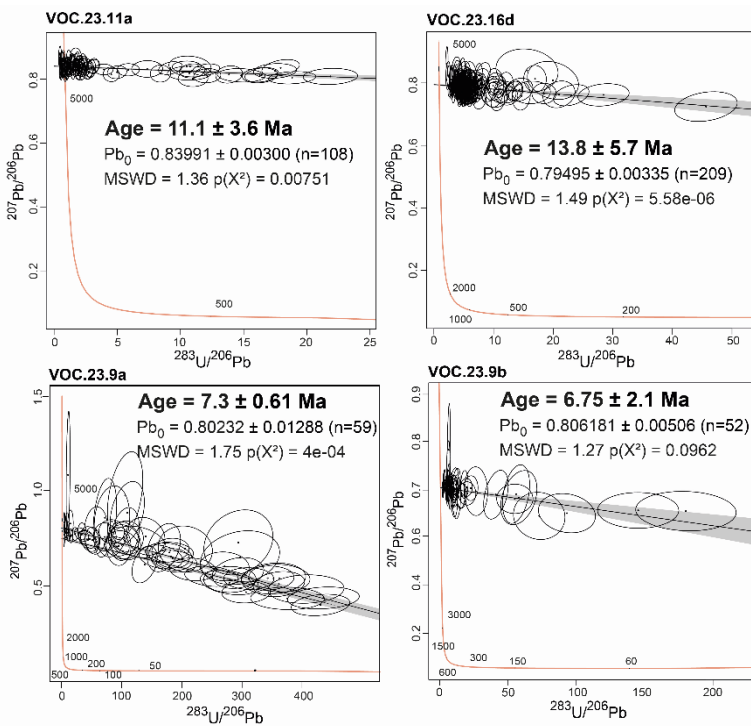


Figure 10: U-Pb on calcite dating results from 12 to 7 Ma.

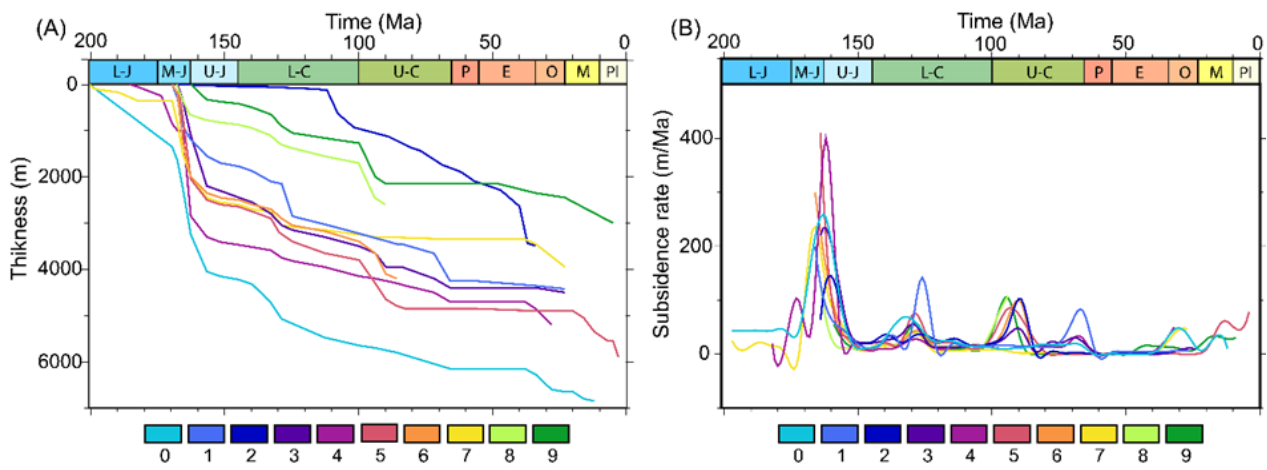
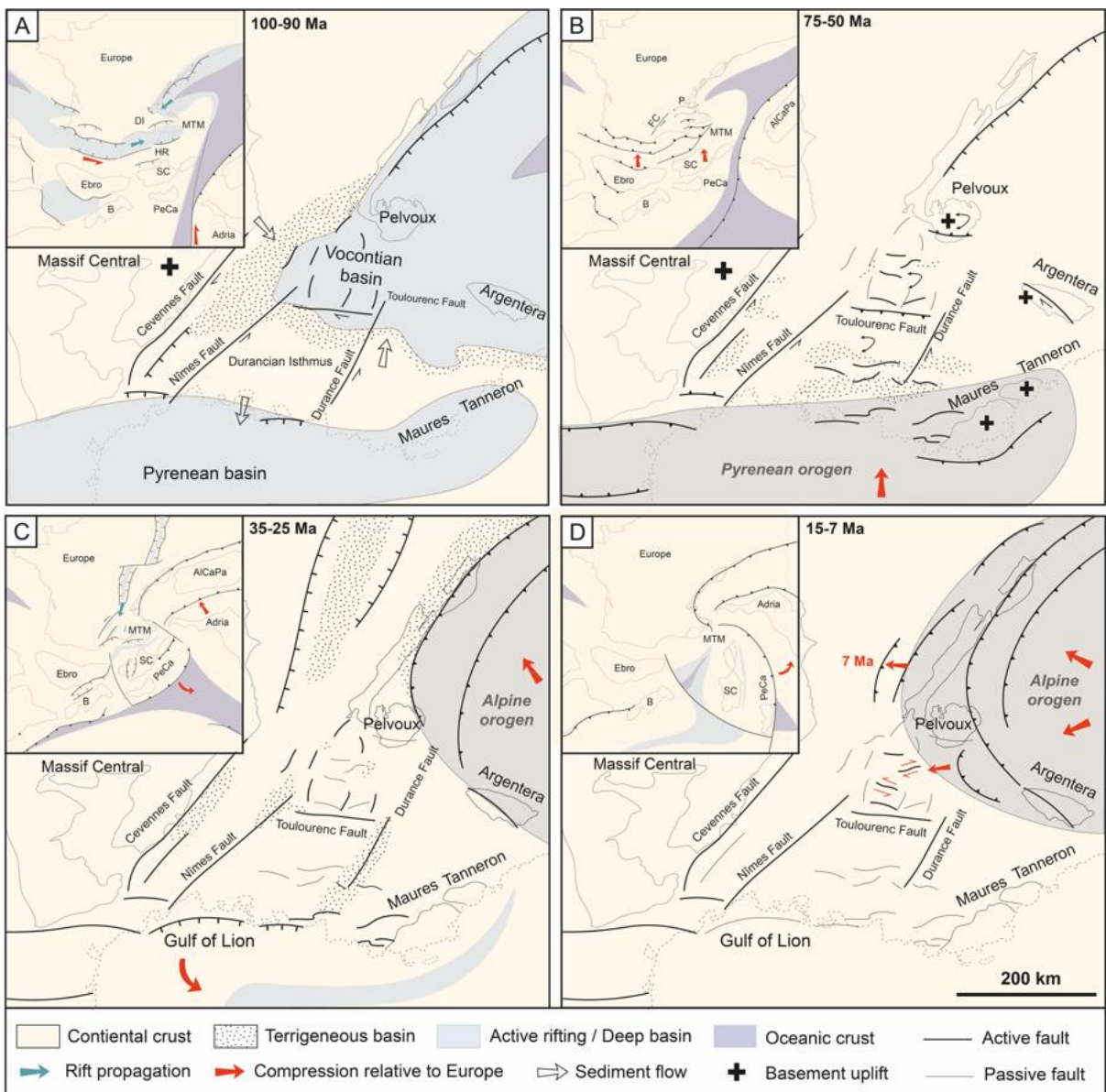


Figure 11: A) Burial history computed after the synthetic stratigraphic sections shown in Figure 10. B) evolution of sediment accumulation rate through time. 0: Die; 1: Dieulefit; 2: Gap; 3: Laragne-Montéglion; 4: Luc-en-Diois; 5: Mens; 6: Nyons; 7: Séderon; 8: Serre; 9: Vaison-la-Romaine. L: lower; mi: middle; u: upper; J: jurassic; C: cretaceous; p: Paleocene; e: Eocene; o: Oligocene; m: Miocene; pl: Pliocene.

1195
1196
1197
1198
1199
1200
1201

1202
1203
1204
1205
1206
1207
1208
1209
1210
1211



1221

1223

1224

Figure 12: Regional tectonic and paleogeographical reconstructions of SE France showing the evolution of the Vocontian basin since the Middle Cretaceous (modified after Boschetti et al., 2025b). A) Rifting in overlapping Pyrenean-Vocontian rift segments at 110-90 Ma. B) Pyrenees-Provence collision phase from 75 to 50 Ma. C) Opening of the West European Rift and onset of Alpine foreland fold and thrust belt tectonics. D) Alpine collision and westward propagation of deformation front. SC: Corsica-Sardinia; B: Balearics; C: Chartreuse; V: Vercors.

1225

1226

Table 1: Calcite sample types and corresponding measurements and ages.

Sample	Lat	Long	Structures	n	$\sigma 1$	$\sigma 2$	$\sigma 3$	ϕ	U-Pb (Ma)	Error (Ma)
VOC.23.01a	44.159326	5.049163	Vein + Strike slip	-	-	-	-	-	76.5	3.4
VOC.23.02b	44.159326	5.049163	Vein	-	-	-	-	-	82.9	3.8
VOC.23.9a	44.190622	5.47628	Strike-slip (Reverse)	13	02/124	80/025	10/214	0.6	7.3	0.61
VOC.23.9b	44.190622	5.47628	Vein (Associated 9a)	11	73/098	16/291	04/200	0.5	6.75	2.1
VOC.23.11a	44.367914	5.352686	Strike-slip (Post-fold)	6	17/0.23	71/185	05/292	0.5	11.1	3.6
VOC.23.12a	44.437467	5.293520	Vein	-	-	-	-	-	25.6	1.3
VOC.23.12b	44.437467	5.293520	Vein + Strike slip	17	10/292	78/078	06/201	0.5	23.2	1.3
VOC.23.13b	44.417889	5.657694	Normal fault	14	78/069	05/315	10/223	0.5	30	2.8
VOC.23.14a	44.328944	5.631972	Vein (Associated 14b)	-	-	-	-	-	34.3	1.5
VOC.23.14b1	44.328944	5.631972	Strike-slip (Normal)	6	17/197	73/007	03/106	0.5	30.3	1.5
VOC.23.14b2	44.328944	5.631972	Strike-slip (Normal)	6	17/197	73/007	03/106	0.5	28.1	1.2
VOC.23.16d	44.575833	5.640667	Strike-slip (Reverse)	20	04/048	86/234	00/138	0.5	13.8	5.7
BON.23.01a	44.62582	5.60985	Plane from fold	11	36/205	04/112	54/017	0.27	72	3.7
BON.23.01	44.62582	5.60985	Plane from fold	11	36/205	04/112	54/017	0.27	71.2	8.1
BON.23.01	44.62582	5.60985	Vein	11	36/205	04/112	54/017	0.27	50	4.3
GLAN.23.02	44.68617	5.59384	Normal fault	4	62/203	04/300	27/032	0.5	27.6	3.4

1227

1228

1229

Table 2: Raman Thermometry data.

Sample	Lat °N	Lon °E	Stratigraphic Age (Ma)	Log/Map	Burial T (30°C/km)	Burial T (60°C/km)	RSCM T (°C)	1s
VOC.23.02	44.556889	5.772778	142	Gap	52	104	<100	
VOC.23.03	44.546834	5.801242	156	Gap	57	114	<100	
VOC.23.05	44.354736	5.668139	135	Serres	51	102	<100	
VOC.23.06	44.296138	5.281886	142	Nyons	51	102	<100	
VOC.23.07	44.299667	5.312604	142	Nyons	51	102	<100	
VOC.23.08	44.227526	5.433728	137	Sederon	75	150	<100	
VOC.23.10	44.221778	5.429244	142	Sederon	77.5	155	<100	
VOC.23.13	44.417889	5.657694	124	Serres	34.5	69	<100	
VOC.23.16	44.575833	5.640667	142	Luc-en-Diois	61.5	123	<100	
VOC.24.17	44.681803	5.414283	167	Mens	122	245	100	20
VOC.24.18	44.698656	5.419786	166	Mens	105	211	120	20
VOC.24.20	44.502694	5.820133	156	Gap	57	114	100	20
VOC.24.21	44.464336	5.697017	157	Luc-en-Diois	69	138	120	20
VOC.24.22	44.316244	5.959372	169	Laragne-Monteglin	93	186	120	20
VOC.24.23	44.308639	5.956206	166	Laragne-Monteglin	73	147	265	12
VOC.24.24a	44.281517	6.014347	163	Laragne-Monteglin	58.5	117	180	20
VOC.24.25	44.294617	6.056911	162	Laragne-Monteglin	58.5	117	228	22
VOCY.24.28a	44.328152	6.128097	170	Laragne-Monteglin	108	216	140	20
VOC.24.29	44.335796	6.020728	166	Laragne-Monteglin	73	147	140	20
VOC.24.31	44.357159	6.166843	175	Laragne-Monteglin	>108	>216	275	6

1231

1232

1233

1234

1235

1236

1237

1230

1238
1239
1240
1241
1242
1243
1244
1245
1246
1247
1248
1249
1250
1251
1252
1253
1254
1255
1256
1257
1258
1259
1260
1261
1262
1263
1264
1265
1266
1267
1268
1269
1270
1271
1272
1273
1274
1275
1276
1277
1278
1279
1280
1281
1282
1283
1284
1285
1286
1287

1288
1289
1290
1291
1292
1293
1294
1295
1296
1297
1298
1299
1300
1301
1302
1303
1304
1305
1306
1307
1308
1309
1310
1311
1312
1313
1314
1315
1316
1317
1318
1319
1320
1321
1322
1323
1324
1325
1326
1327
1328
1329
1330
1331
1332
1333
1334
1335
1336
1337

1338
1339
1340
1341
1342
1343
1344
1345
1346
1347
1348
1349
1350
1351
1352
1353
1354
1355
1356
1357
1358
1359
1360
1361
1362
1363
1364
1365
1366
1367
1368
1369
1370
1371
1372
1373
1374
1375
1376
1377
1378
1379
1380
1381
1382
1383
1384
1385
1386
1387

1388
1389
1390
1391
1392
1393
1394
1395
1396
1397
1398
1399
1400
1401
1402
1403
1404
1405
1406
1407
1408

1409

1410
1411
1412
1413
1414
1415
1416
1417
1418
1419
1420
1421
1422
1423
1424
1425
1426
1427
1428
1429
1430
1431
1432
1433
1434
1435

1436
1437
1438
1439
1440
1441
1442
1443
1444
1445
1446
1447
1448
1449
1450
1451
1452
1453
1454
1455
1456
1457
1458
1459
1460
1461
1462
1463
1464
1465
1466
1467
1468
1469
1470
1471
1472
1473
1474
1475
1476
1477
1478
1479
1480
1481
1482
1483
1484
1485

1486
1487
1488
1489
1490
1491
1492
1493
1494
1495
1496
1497
1498
1499
1500
1501
1502
1503
1504
1505
1506
1507
1508
1509
1510
1511
1512
1513
1514
1515
1516
1517
1518
1519
1520
1521
1522
1523
1524
1525
1526
1527
1528
1529
1530
1531
1532
1533
1534
1535

1536
1537
1538
1539
1540
1541
1542
1543
1544
1545
1546
1547
1548
1549
1550
1551
1552
1553
1554
1555
1556
1557
1558
1559
1560
1561
1562
1563
1564
1565
1566
1567
1568
1569
1570

1571
1572
1573
1574
1575
1576
1577
1578
1579
1580
1581
1582
1583
1584
1585
1586
1587
1588
1589
1590
1591
1592